UNDERSTANDING THE MACROSCOPIC PROPERTIES OF POLYMER GRAFTED NANOPARTICLES BY MESO-SCALE MODELING

A Dissertation

Presented to the Faculty of the Graduate School

of Cornell University

In Partial Fulfillment of the Requirements for the Degree of

Doctor of Philosophy

by

Sushmit Sunil Kumar Goyal

Jan 2017

UNDERSTANDING THE MACROSCOPIC PROPERTIES OF POLYMER GRAFTED NANOPARTICLES BY MESO-SCALE MODELING

Sushmit Sunil Kumar Goyal, Ph. D

Cornell University 2017

Polymer nanocomposites have been a topic of interest in recent years for their potential in applications such as water desalination, CO2 capture, photovoltaics, battery membranes and immersion lithography. Unlike colloids which tend to agglomerate irreversibly, polymer grafted colloids are stabilized by polymer-polymer steric interactions. Polymer grafted nanoparticles(PGNs) are a class of such materials which consist of an inorganic nanoparticle core, functionalized with a corona of organic oligomers. These differ from common nanocomposites in that the tethered corona can be used as the sole suspending medium for the cores. The hybrid nature of the suspension allows the fabrication of materials with tunable properties by varying parameters such as nanoparticle chemistry, shape and size, as well as the polymer molecular weight, grafting density and chemistry. The range of properties exhibited by these composites vary from solids, stiff waxes, and gels for high core content to single component solvent free fluids for low core content.

While PGNs have been extensively studied experimentally by several groups at Cornell, this research focuses on the use of molecular simulations to help elucidate the effect of molecular design on the properties of PGNs. We studied the effect of grafting density,

corona thickness and core volume fraction on equilibrium and non-equilibrium properties like diffusivity, rotational diffusivity, equilibrium structure, rheology and molecular origin of stress. We find that increasing the chain length and grafting density decreases the viscosity and structural order, which makes the system to have a more liquid-like behavior. While these trends have also been observed in experiments and predicted by analytical theories, our results complement simulations data from other groups to provide a molecular basis for these phenomena and to create phase diagrams to encapsulate the behavior of a large number of systems.

We also compare the properties of solvent-free PGNs with those suspended in a solvent, and examine the effect of dilution in these systems. We find that solvent-free systems have higher viscosity and a larger shear thinning coefficient. On studying the phase behavior of PGNs in chemically identical polymeric solvents, we find that changing the ratio of polymer length to nanoparticle size can result in a transition from well-mixed systems to phase-separated systems, a phenomenon that could be attributed to the interplay between entropic forces acting on the grafted and free polymers. Our simulations reveal trends in structural packing for low curvature PGNs that are consistent with those observed in experiments and predicted by theory (e.g., as pertaining to the first peak of structure factor), while predicting that for high curvature PGNs macrophase separation can occur (a trend yet to be tested experimentally).

BIOGRAPHICAL SKETCH

Sushmit Goyal was born and brought up in Bikaner, India. He completed his undergraduate in Chemical Engineering with a minor in Mathematics for Computer Science in 2004 from Indian Institutive of Technology Madras, Chennai, India in 2009. In August 2009 he joined Cornell University to pursue a PhD in Chemical and Biomolecular Engineering. Over the last 6 years he was worked on the meso-scale modeling of polymer grafted nanoparticles(PGNs). He has studied the effect of molecular design on the structure, rheology and phase behavior of self-suspended and solvated PGNs. He has also worked on the rheology of hard colloidal particles under the action of oscillatory shear.

I dedicate my thesis to my parents for their never ending support, constant encouragement and unconditional love.

ACKNOWLEDGMENTS

I would like to thank Dr. Fernando Escobedo, Dr. Donald Koch and Dr. Rosseana Zia for the guidance and support they have provided me in the past 6 years. Dr. Escobedo is one of the best teachers I have had the pleasure of learning from and his graduate thermodynamics and kinetics course never failed to amaze me and encouraged me to learn more about them. He has also been an excellent mentor helping me better myself in every way. Dr. Koch has always amazed me with his knowledge of colloidal science and his humble approach to research. Working on a project with Dr. Zia and being a TA for her undergraduate course was one of the most enjoyable and enriching time of my graduate school.

I had the pleasure of have great coworkers like Umang and Carlos who helped me learn the nuances of research. Vikram, who is a great friend, a very knowledgeable colleague and also a great person to spend time discuss sports. Pooja and Poornima would always keep the lab lively and a very fun place to work in.

Finally, I would also like to thank my dearest friend Srinitya for supporting me all throughout my graduate school and enriching my life in every way. Winter in Ithaca always felt warm in her company.

TABLE OF CONTENTS

LIST OF FIGURES

LIST OF TABLES

1 Introduction

Dispersion of inorganic nanoparticles in polymers to form polymer nanocomposites has been a topic of interest in recent years due to their enhanced mechanical properties. Their unique properties have been exploited for applications such as desalination, CO2 capture, photovoltaics, and immersion lithography[1-4]. One of the common problem with such an approach is the irreversible agglomeration of nanoparticles due to either the enthalpic interaction between nanoparticle surfaces or from the depletion attraction resulting from the entropic gains associated with the expulsion of solvent in between nanoparticles. Polymer grafted nanoparticles (PGNs) are a class of material in which the polymer chains are grafted directly to the surface of nanoparticles (also called corona) which introduces steric repulsion and stabilizes the system. PGNs can be solventless, where the grafted chains fill in the space between the nanoparticles to form the suspending fluid phase[2-6], or solvated with identical or different solvent[7,11]. The hybrid nature of the suspension allows for very rich physical properties ranging from solids, stiff waxes and gels for suspensions with high nanoparticle content, to low viscosity fluids for low nanoparticle content[4-6]. The variation in physical properties can be controlled by tuning the nanoparticle (such as chemistry, shape, and size) and the grafted and free polymer (such as molecular weight and grafting density).

Given the different ways in which a single PGN can be modified, molecular simulations can help elucidate their effect on bulk properties (and can be optimized for specific applications), by changes in molecular design. Multiscale simulations are required to understand the properties of PGNs as different simulation models reveal difference

physics; this is shown pictorially in figure 1.1. These models would vary from all atom models, which would predict the microstructure and potential of mean force (PMF) between the particles to mesoscale models which can be used to study the bulk behavior.

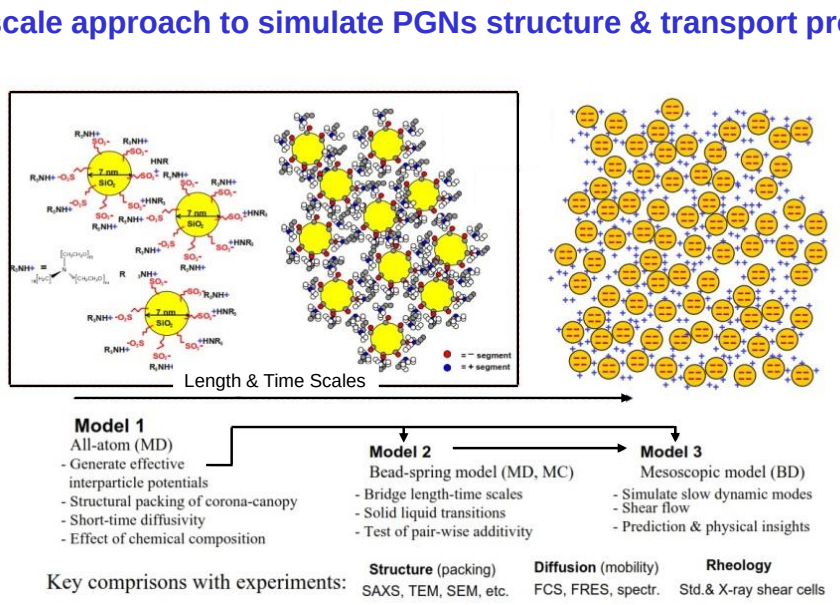

Figure 1.1 The various simulation models which can be used to understand the structure and transport properties of PGNs.

In the study presented here, we are interested in the structure, rheology and phase behavior for PGNs and hence we use mesoscale modeling.

For solventless PGNs systems, understanding the structural distribution and response to stress (or rheology) is particularly interesting, such a study can help us understand the transition from solids to free fluids due to absence of external suspending agent .Experimental studies have been carried out to understand the rheology of such systems

and discovered the occurrence of shear thinning and a Newtonian plateau for low shear rates, the viscosity was also found to decrease with increasing polymer chain length [3]. Density function theory using space filling constraints has shown that every nanoparticle excludes exactly one other particle which implies that each nanoparticle carries its suspending fluid along with it [5]. Molecular simulation studies of these systems have shown the different morphologies that can be observed by varying the grafted chain length, grafting density, and nanoparticle size [12]. Coarse grained simulations have shown the phase separation of these systems into finite striped, long stripes and percolated systems [65]. The literature however, does not answer key questions such as effect of PGN structure on equilibrium properties, viscosity and origin of its shear thinning.

Solventless PGNs are limited in the range of grafted chains length and grafting density that can form stable suspensions. The addition of solvent can allow stabilization of previously aggregated PGNs and give us more flexibility in design and hence in creating composites with desirable properties. Comparison of solvated and solventless PGNs can give insight into the unique effect of grafted solvent on physical properties. Multiple stable PGNs can be created by choosing the same amount of nanoparticles and polymers and by grafting different amounts to the nanoparticle leaving the remaining polymers in solvent. Comparison between such systems can answer many interesting questions like what is the difference in structure and viscosity, do they all shear thin and if so is the shear thinning slope the same? We try to answer these questions posed by solventless and solvated PGNs in chapter 2.

To study the phase behavior of PGNs, we need to understand the factors that stabilize such a suspension. PGNs dispersed in solvent is characterized by the interpenetration of solvent into the grafted chains leading to stabilization of the suspension(wetting), or their expulsion causing nanoparticles to aggregate (dewetting) [7]. The solvent used for dispersing the PGNs can be chemically identical or different to the grafted chains. Using solvents that have an affinity for grafted chains is a common method to leverage enthalpy to form stable suspension and have been studies via experiments and simulations [55-60]. Due to the absence of enthalpic driving forces, PGNs in chemically identical solvent form an interesting model system as the wetting/dewetting phenomenon is purely entropic in nature. Experimental studies show that for such systems, decreasing the ratio of solvent molecular weight to grafted chain molecular weight , increasing the number of chains attached to the nanoparticle (grafting density), and increasing the polydispersity in grafted polymer weight favors formation of well dispersed systems. Theoretical studies approximate the PGNs as flat surfaces with grafted chains show that wetting-dewetting behavior is governed by the change in translational entropy of the solvent. Shorter solvent chains can interpenetrate grafted chain to maximize their translational entropy while for longer solvent chains; the decrease in entropy of the grafted chains is enough to make this transition unfavorable [61,62]. Simulations have further shown that the dewetting behavior can be attributed to the transition in potential of mean force between two PGNs from repulsive to attractive [8,9,41].

Recent experimental work has revealed that there exist a vast number of systems for which theory for flat brushes would expect phase separation, are actually well dispersed

and form stable suspensions. This was attributed to the curvature of nanoparticles which increases the possibility of solvent chains to interpenetrate grafted chains and modifies the steric forces experienced by the grafted chains [49,50]. This in turn affects the entropic interactions between the grafted chains and the free chains thus the region for wetting. Hence, to understand the phase behavior of PGNs, it is essential to account for the curvature of the nanoparticles. Analytical work using polymer mean field theory for two PGNs has extended the wetting behavior from flat brushes to curved particles giving guidelines for calculation properties like the interpenetration width between solvent and grafted chains [69]. It was also found that grafting density had a small impact on wetting behavior while curvature had a more pronounced effect. PRISM theory, density functional theory and molecular dynamics has been used to predict bulk behavior by calculate PMF for two nanoparticles in solvent and outlines the effect of solvent chain length and grafting density on dispersion. As all studies have been focused on single particle or two particles in identical polymer melt and do not capture all multibody effects of a bulk suspension. Therefore there is a need to understand the effect of curvature on densely grafted PGNs using bulk simulations. Also, do all PGNs with wetted grafting chains form stable colloidal systems? In chapter 3 we try to address these questions and explore the effect of curvature of phase behavior of PGNs.

Finally in chapter 4, we present a summary of this work and present some ideas which could give novel polymer nanocomposites with desirable properties.

2 Structure and Transport Properties of Polymer Grafted Nanoparticles

Adapted with permission from S. Goyal, and F. Escobedo, Structure and transport properties of polymer grafted nanoparticles, *The Journal of Chemical Physics*, 135, 18904 (2011)

2.1. Introduction.

Polymer nanocomposites have been a topic of interest in recent years as their unique properties have been exploited for applications such as desalination, CO_2 capture, photovoltaics, and immersion lithiography.[1-4] Unlike colloids which tend to agglomerate irreversibly, suspensions of polymer grafted nanoparticles (PGNs) are stabilized by polymer-polymer steric interactions. Nanoscale organic hybrid materials (Nohms), which are a class of such materials, consist of an inorganic nanoparticle core, functionalized with a corona of organic oligomers. These differ from common nanocomposites in that the tethered corona is the suspending medium for the cores;[2-6] the grafted polymers tend to fill in the space between the inorganic cores to form the suspending fluid "phase" (as shown in schematic 1). The hybrid nature of the suspension allows the fabrication of materials with tunable properties by varying parameters of both the organic polymers (such as molecular weight and grafting density) and the nanoparticle cores (such as chemistry, shape, and size). The properties exhibited by these composites vary from solids, stiff waxes, and gels for systems of high core content to solvent free fluids[4-6] for systems of low core content.

Theoretical, experimental, and computational studies have been carried out to elucidate the transport properties of polymer grafted nanoparticles in a polymer matrix;[1,7-11] a

wetting regime was identified where the surrounding polymer matrix interpenetrates the grafted nanoparticles, effectively wetting and stabilizing them. Various theoretical and computational studies have also been carried out on the structural effect of tethering chains, chain length, and tether location.[5, 8, 9] For pure PGN systems, various experimental studies have been carried out to characterize the rheology of brush-type PGNs where the thickness of grafted polymers is comparable to the nanoparticle radius, finding a distinctive shear thinning behavior and a marked influence of polymer chemistry on viscosities. [3] Molecular simulation studies of these systems have been initiated only very recently.[12]

Given the different ways in which a single PGN can be modified, molecular simulations can help elucidate how their bulk properties are affected (and can be optimized for specific applications), by changes in molecular design. To this end, we have applied Molecular Dynamics to get a better understanding of structure and transport properties of these systems. In this work we investigate the equilibrium and rheological properties of PGNs. The simulated systems were chosen to roughly mimic some experimental systems made of silica cores and PEO chains (having high grafting density and short chains [2]) and to isolate the contributions of core and corona on PGN's dynamics by varying the core volume fraction and polymer length. PGNs with varying core density and corona size were hence simulated wherein non-equilibrium methods were implemented to obtain both viscosities (by imposing a homogeneous steady state shear) and the yield stress. A non-Newtonian shear thinning behavior is observed in all cases with a lower shear thinning slope for PGNs in a blend as compared to pure PGNs.

In the next section we introduce our model (section 2) followed by the methodology used to calculate the system's properties (section 3). We then present and analyze our results in section 4 and give some concluding remarks in section 5.

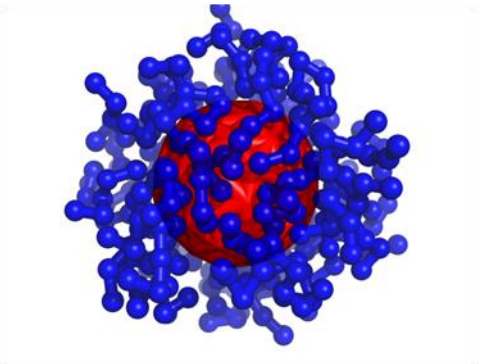

Figure 2.1. Schematic of a typical PGN.

2 Model

Figure 2.1 represents a schematic of a single PGN particle. The nanoparticle component is modeled as a hollow spherical shell made of 80 Lennard Jones (LJ) beads forming the surface and a single bead in the center. All LJ beads have a diameter of σ which gives the nanoparticle core an outer diameter of $D = 6\sigma$ (Fig. 2a). To fix the LJ beads on a spherical surface, each bead on the surface is attached to its neighboring beads and also to the center bead by harmonic bonds (Fig. 2b & 2c). These surface LJ beads are used as grafting points to permanently anchor polymers to the surface of the nanoparticle. Tethered polymers are freely jointed chains of N_m beads. For the blend system (PGNs + polymer melt), the surrounding fluid has chains of N_{fp} beads each and the ratio of number of tethered chain beads to number of free chain beads is given by P_f.

For computational efficiency, we coarse grained our system to reduce the number of particles required. We have not used the usual dissipative particle dynamics soft potential as it contains only repulsive interactions which would not capture non-ideal chain conformational behavior arising from attractive interactions and the non-crossability of chains. We have instead used a coarse grained chain model with Lennard Jones beads and stiff bonds noting that a N_m-bead oligomer could not only represent a chain with N_m Kuhn segments but also approximate a bundle of a few oligomer chains. To roughly map LJ units into real units, a value of $\sigma \approx 1$nm can be estimated by mapping the core diameter to the smallest diameter of silica particles typically used experimentally.[2, 6]

The grafting density (GD) gives what percentage of the maximum possible number of chains has been attached to the nanoparticle surface. It is calculated in our model as

$$\text{GD} = \frac{\#\text{ of chains attached}}{\#\text{ of surface beads}} \times 100 . \qquad (1)$$

When GD<100, grafting points are chosen randomly from the 80 surface beads so as to produce a relatively uniform coverage. The volume fraction of cores (ϕ_c) is calculated as

$$\phi_c = \frac{(\text{number of cores}) \times \frac{\pi}{6} D^3}{\text{Volume of simulation box}} . \qquad (2)$$

Figure 2.3(a) and 2.3(b) show snapshots of some of the systems simulated and Fig. 2.3(c) and table 1 summarize the key characteristics of the systems simulated in this study.

To identify the various simulated systems we use a three variable naming scheme where we represent each system using the formulae N_m-GD-ϕ_c , which gives the chains length(N_m), grafting density (GD) and core volume fraction (ϕ_c). For the case when we have simulated a blend, we use the formula N_m-GD-ϕ_c (N_{fp}-P_f) , which specifies the needed additional parameters, namely, chain length (N_{fp}) of free polymers and volume ratio of free chains to total chains(P_f).

The pair interaction potential used between non bonded beads is the cut-shifted Lennard Jones force potential which gives a continuous potential and force, the potential is given as [13].

$$v^{sf} = \begin{cases} v - v_{cutoff} - (r - r_c)\left(\frac{dv}{dr}\right)_{r_c}, & r_{ij} < r_c \\ 0, & r_{ij} > r_c \end{cases}$$
$$v = 4\varepsilon\left[\left(\frac{\sigma}{r}\right)^{12} - \left(\frac{\sigma}{r}\right)^{6}\right] \qquad (3)$$
$$v_{cutoff} = v \quad \text{for } r = r_c$$

Where v is the Lennard Jones potential and r_c is the cutoff distance which is taken as $2^{1/6}$ for surface-surface beads and 2.5 between polymer-polymer beads and between surface-polymer beads. The interaction parameter ε is 1 for surface-surface and polymer-polymer bead interactions and 0.5 for surface-polymer bead interactions.

Bonded interactions are taken to comprise of terms with 2nd and 4th power of the distance between bonded beads:

$$v_{ij} = \frac{1}{2}k_1(r_{ij} - r_{eq1})^2 + \frac{1}{4}k_2(r_{ij} - r_{eq2})^4 \qquad (4)$$

Where, the 2nd power term gives a suitable description of the potential at small deviations from equilibrium bond lengths while the 4th power term which dominates at larger deviations gives a stiffer restoring force at these distances. The values of r_{eq1}, r_{eq2}, k_1 and k_2 are 2.47, 2.57, 500 and 60000 for center and surface beads; 0.97, 1.07, 500 and 40000 for both surface-polymer and polymer-polymer beads; and 1.00, 1.09, 300 and 40000 for surface-surface beads, respectively. To prevent chains from penetrating into the cores, the core center bead and chain beads interact via a repulsive potential: $v = 500(r - 2.5)^2$ for r<2.5, and v=0 otherwise.

System	N_m	GD	ϕ_c	Number of cores	L_{box} Box length
A	5	80	0.23	256	50.41
A-100	5	100	0.19	256	53.41
A-50	5	50	0.32	256	45.10
B	10	80	0.13	256	61.25
B-50	10	50	0.19	256	53.55
C	20	40	0.13	108	45.93

Blend	N_m	P_f	ϕ_c	Number of cores	N_{fp}	L_{box}
D	5	0.5	0.13	108	5	45.93

Table 2.1. Simulation parameters of the various systems studied.

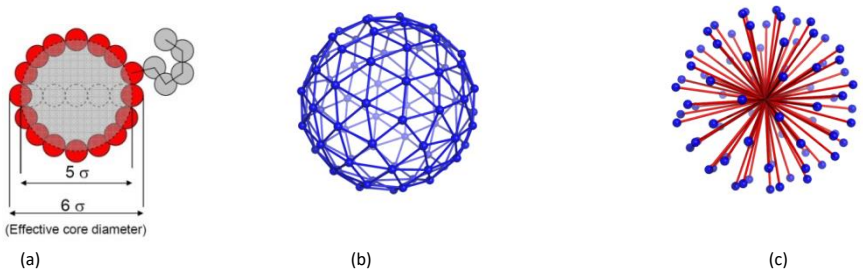

Figure 2.2. Schematic of (a) approximate dimensions of PGNs (b) Surface beads and bonds joining neighboring particles without center bead. (c) Core structure showing center bead and bonds with surface beads.

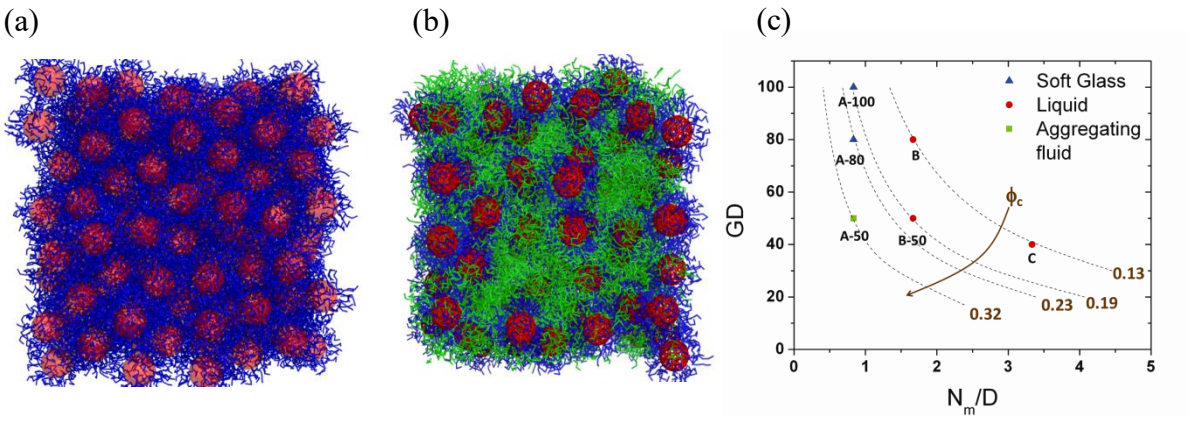

Figure 2.3. Snapshots of sample simulated systems (a) System A with ϕ_c=0.23, N_m=5, and GD=80% (b) System D, PGNs in blend with polymer with ϕ_c=0.13, N_m=5, and N_{fp}=5 (c) Summary of pure PGN systems explored in the GD vs N_m/D space with isolines shown for different ϕ_c values. The meaning of the symbol legends are described in Sec. 4.

We used reduced LJ units with $T^* = \frac{k_B T}{\varepsilon}$, $P^* = \frac{P\sigma^3}{\varepsilon}$, and $\rho^* = \frac{N}{V}\sigma^3$ throughout and employ an in-house Molecular Dynamics code which implements the velocity Verlet algorithm where temperature is kept constant at T^*=1.0 using the Lowe-Andersen thermostat with the coupling constant (fraction of collision pairs whose velocities are adjusted at each time step) set to 0.0003. The Lowe-Andersen thermostat is used to preserve hydrodynamic interactions.[14] The equilibration pressure was $P^* \approx 0.2$ for systems B, C and D, and $P^* \approx 0.7$ for systems A (i.e., A-100, A, and A-50); this is done to always have a number density for the fluid of ~0.82 (defined as the ratio of number of chain beads to the volume not occupied by the cores); i.e., a suspending polymer media of equal density as is the case in experiments. All systems were pre-equilibrated by using the Berendsen barostat with a coupling constant as 0.0005 and volume moves enacted after every 15 steps. The time step for simulations is Δt=0.005.

3. Evaluation of Properties

3.1 Corona thickness and Interdigitation.

The corona thickness, ξ, is estimated as the distance from the nanoparticle surface at which 90% of the grafted chain beads are found. This is illustrated in Fig. 4a for systems A and C, showing that longer chains have wider, longer-tailed distributions than shorter chains. Interdigitation, a measure of overlap between chains of neighboring particles with respect to corona thickness, is defined as:

$$Interdigitation = 2 - \frac{(D_1 - D)}{\xi} \qquad (5)$$

Where D_1 is the distance between neighboring cores which is calculated from the location of the first peak of the core-core radial distribution function (Fig. 4a); $D_1 - D$ is the distance between core surfaces.

3.2 Pair distribution functions

Three radial distribution functions of interest are the core-core, $g_{cc}(r)$, core-grafted polymers, $g_{cg}(r)$ and core-free polymers, $g_{cf}(r)$. These functions are defined as follows

$$g_{\alpha\beta}(r) = \frac{\#\text{ of } \beta \text{ type particles at distance } r \text{ from } \alpha}{\#\text{ of ideal gas particles at distance } r \text{ from } \alpha} \qquad (6)$$

For the calculation of $g_{cg}(r)$ and $g_{cf}(r)$, the denominator contains the number of ideal gas particles in the volume element at distance r that is available for chains to occupy. This volume is obtained by subtracting the volume occupied by nanoparticle cores from each volume element at distance r as shown in figure 2.4c.

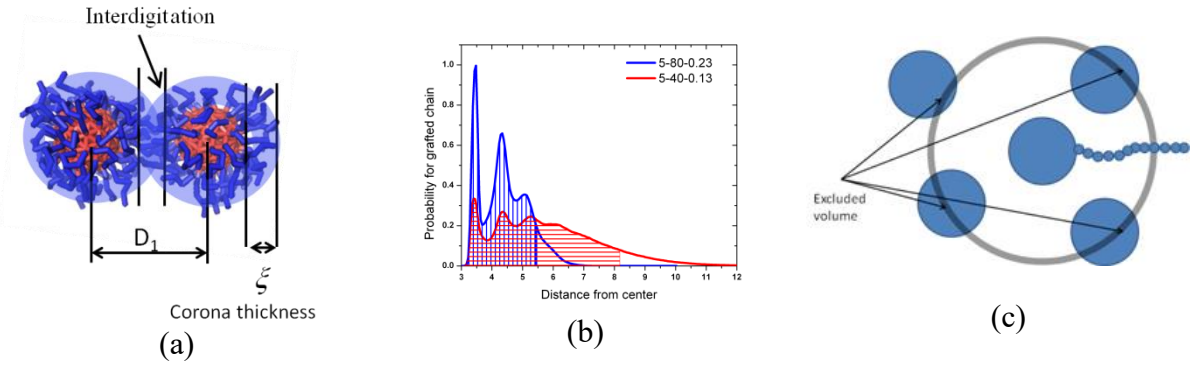

Figure 2.4. Schematic of (a) Corona thickness and interdigitation in PGN's (b) probability of finding grafted chain bead from surface of nanoparticles for short and long chains.(c) Volume excluded for calculation of $g_{\alpha c}(r)$ (for $c \neq \alpha$)

3.3 Diffusion

Translational and Rotational diffusivities for various PGN's are calculated by the Stokes-Einstein and Stokes-Einstein-Debye relations [15-17] which are given by

$$D_{t,calculated} = \lim_{\Delta t \to \infty} \frac{1}{6\Delta t} \left\langle r^2(\Delta t) \right\rangle$$
$$D_{r,calculated} = \lim_{\Delta t \to \infty} \frac{1}{4\Delta t} \left\langle \varphi^2(\Delta t) \right\rangle \qquad (7)$$

The terms r^2 (Δt) and $\varphi^2(\Delta t)$ are the mean squared displacement for position and orientation (angle) respectively. The translational motion is measured by tracking the center of core particles. For the calculation of rotational diffusivity we define a principle unit vector which extends from the center of the nanoparticle to a fixed bead on the surface ($\vec{p}_i$). The rotation is tracked by the vector angle traced by ($\vec{p}_i$) in time Δt, the magnitude of which is given by $\cos^{-1}(\vec{p}_{i,t}.\vec{p}_{i,t+\Delta t})$ and direction by $\vec{p}_{i,t} \times \vec{p}_{i,t+\Delta t}$. As the cosine function is periodic, we cannot distinguish between rotations of θ and (2π+θ) and therefore we calculate $\vec{\varphi}$ by adding the rotation vectors $\delta\vec{\varphi}$ for every time interval between 0 and t to obtain the net angle using

$$\vec{\varphi}(t) = \int_0^t (\delta\vec{\varphi}) dt' \qquad (8)$$

For a system in diffusive regime, the distribution of particles is given by the Van Hoove distribution and the deviation from this is quantified by using the nongaussianity parameters

$$\alpha_2(t) = \frac{3\langle \varphi^4(t) \rangle}{5\langle \varphi^2(t) \rangle^2} - 1$$

$$\alpha_2(t) = \frac{3\langle r^4(t) \rangle}{5\langle r^2(t) \rangle^2} - 1$$

for rotation and translation respectively. Non gaussianity parameter increases from ballistic to sub diffusive regime and attains maxima when system enters diffusive regime. We used the location of the peak of this function to identify crossover to diffusion for our systems.[18]

The absolute diffusivity values reported are in reduced LJ units. To facilitate comparison to experiments, a ratio of the calculated diffusivity is taken with respect to the ideal diffusivity of an identical nanoparticle (core) in a polymer melt as calculated by the Stoke Einstein and Stoke Einstein Debye relations given by

$$D_{t,ideal} = \frac{k_B T}{6\pi\eta R};\ D_{r,ideal} = \frac{k_B T}{8\pi\eta R^3} \qquad (9)$$

where T is the temperature, η the zero shear viscosity of the fluid, k_B the Boltzmann constant, R the radius of nanoparticle, and the polymer melt is taken to consist of chains of the same length as those grafted to the PGNs. We refer to this ratio of diffusivity to ideal diffusivity as the relative diffusivity:

$$D_t = \frac{D_{t,\mathrm{calc}}}{D_{t,ideal}};\ D_r = \frac{D_{r,\mathrm{calc}}}{D_{r,ideal}} \qquad (10)$$

3.4 Constant-rate uniaxial extension

Simulations that probe the dynamic response of the system to a uniaxial deformation have often been used to characterize the strength and failure of adhesives and glassy polymers.[19-21] We implemented this technique in our system having periodic boundary conditions (along all axes) by gradually elongating the box along the *z*-axis while keeping the *xy* cross section constant. The system starts inside a cubic box and is pre-equilibrated at T^*=1.0 and a density consistent with P^*=0.2. While the dynamic response depends on the strain-rate applied, we adopt here a single rate value of $0.02\,\frac{\sigma}{\Delta t}$ (perturbations enacted every 100 equilibration steps) which is consistent with typical values used with such simulations for polymeric materials.[21] As the box elongates, "volume" is being created which forces the system to eventually become heterogeneous and break-up into filled and empty domains. This constant cross-section uniaxial stretching differs from constant-volume stretching experiments (where the sample is cross-section concertedly reduced); the former is indicated to probe the failure of glassy films with relatively large *xy* cross-section while the former is more suited to probe the elastic response of rubbery materials.

3.5 Viscosities and Yield Stress

For calculating the shear-dependent viscosity of the systems, SLLOD [22, 23], a commonly used NEMD technique is used along with Lees Edwards boundary condition[24]. SLLOD imposes a homogenous steady shear strain on the system and measures the resulting steady state stress. Similar to diffusivities, we reduce the viscosities by a factor η_0 which is the zero-shear viscosity of the melt comprising of chains identical to the grafted

polymers, to obtain relative viscosities $\eta_{rel} = \frac{\eta_{actual}}{\eta_0}$. To relate our results with experiments, we convert shear rates to a ratio of convective motion to diffusive motion given by the Peclet number (Pe) defined as

$$Pe = \frac{6\pi\eta_0\dot{\gamma}R^3}{k_BT} \qquad (11)$$

where $\dot{\gamma}$ is the shear rate and R is the core radius. To estimate yield stresses we use the constant stress algorithm of Hood, Evans and Morriss[25] (using their Equation 3 and adopting a value of $\tau_{y.}$=100 for the feedback response time).

We study the effect of corona thickness and GD on viscosity and yield stress. We vary the corona thickness by changing chain length and GD for pure PGNs. Chain length is varied while keeping ϕ_c constant to help us isolate and understand the effect of corona thickness on both equilibrium and rheological properties.

3.6 Brownian Stress

On application of shear, the flow induced disturbance in the system perturbs the equilibrium structure; the resulting particle diffusion induces a stress.[26] The viscous contribution of this stress is known to reduce with Peclet number thus causing shear thinning. This so-called Brownian stress is calculated by[26-28]

$$n\left\langle S^B \right\rangle = -n^2 k_B T R \int_{r=2a} \hat{r}\hat{r}g(\vec{r})d\Omega \qquad (12)$$

Where, n is the number density of nanoparticles in the system, R is particle radius taken as radius of nanoparticle ($\approx 3\sigma$), $g(\vec{r})$ is the radial distribution function at $\vec{r}$, and $\hat{r}$ is the unit vector of $\vec{r}$. $g(\vec{r})$ is calculated by storing the separation vectors between pairs of particles and creating a histogram of these vectors on a grid of spherical coordinates r, θ and ϕ and normalizing it by the number of ideal gas particles in the same volume element.

$$g(r,\theta,\phi) = \frac{\#\text{ of PGN centers in elemental volume at } r,\theta,\phi}{\#\text{ of ideal gas particles in elemental volume } V(r,\theta,\phi)} \qquad (13)$$

Where $V(r,\theta,\phi) = r^2 \sin\theta dr d\theta d\phi$, we have taken only the contact integral into account as it is known to give an accurate description of the Brownian stress.[26, 27] Equation (12) was developed for colloidal particles suspended in a continuum fluid and hence it is not strictly applicable to pure PGNs; however, it is expected to give a semiquantitative description of Brownian stresses for PGNs given that the grafted chains provide a relatively homogeneous (self-suspending) media for the cores.

3.7 Chain orientation

Due to shear, grafted and free chains (if present) in PGN systems tend to align in the direction of shear; this makes the polymers more streamlined and reduces viscosity.[29,30] To study this phenomenon in our systems, we calculate the angle (θ') made by the end-to-end vector of each polymer with the shear axis (the x axis here, see Fig. 5). A probability distribution for θ' is obtained from

$$f_{\theta'} = \frac{P_{\theta'}}{\sin\theta'} \quad \text{where } P_{\theta'} = \frac{\text{Frequency of angle } \theta'}{\text{Total number of polymers}} \tag{14}$$

P_{θ}' has been divided by $\sin\theta'$ to obtain the ratio with respect to the ideal distribution which is proportional to the solid angle being sample around θ'; i.e., ~$\sin\theta' d\theta' d\phi$. Note that Eq. (14) will produce a flat distribution for an isotropic distribution of angles but will tend to overemphasize $P_{\theta'}$ for small values of sin θ'.

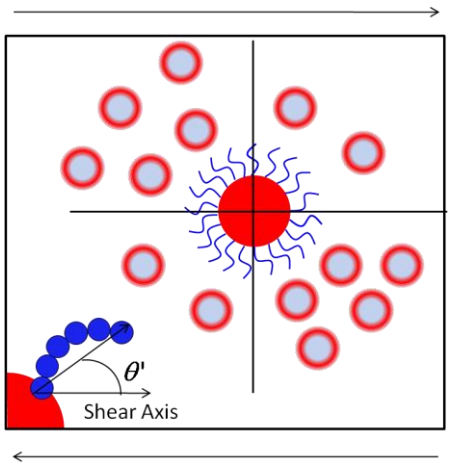

Figure 2.5. Schematic of anisotropic distribution of particles under shear and definition of chain orientation angle under shear θ'.

4. Results and Discussion

4.1 Structure and Diffusivity

To understand the effect of core concentration or ϕ_c, we calculate the relative diffusivity of a single PGN with N_m=5 and GD=80% in a melt of N_m=5, i.e., in our notation it is given by 5-80-0(5-1). The relative diffusivity of this single PGN isolates the effect of tethering chains on the nanoparticle and is not affected by caging or interdigitation. The

value of the relative translational diffusivity is 0.55 for such a single PGN which is much larger than the value of 0.0052 obtained for a system of pure identical PGNs (system A: 5-80-0.19). This shows that with the addition of more cores, the particles get caged and translational diffusivity is reduced. For rotation, the relative diffusivity for a single PGN in the chain melt is 0.36 which is close to the diffusivity of 0.16 for system A, indicating that the friction between tethered chains is only slightly larger than that between tethered and free chains.

We focus next on the effect of corona size for fixed value of core volume fraction. The systems under study are system B (10-80-0.13), C (20-40-0.13) and D [5-80-0.13(5-0.5)], where always ϕ_c=0.13 while tethered chain length varies. Figure 2.6(a) shows the core-core radial distribution functions for these systems. System C shows a very even $g_{cc}(r)$ with a short first peak, consistent with a well dispersed liquid-like system, while system B shows a more pronounced structure (higher peaks and deeper troughs) suggestive of a glassy or solid-like material. System D [5-80-0.13(5-0.5)] constitutes an intermediate case as the free chains can here spread out more evenly than the attached chains in system B. This is also supported by Figure 2.6(b) which shows the distribution of $g_{cc}(r)$, $g_{cg}(r)$ and $g_{cf}(r)$ for system D, where the latter distribution of free chains is observed to be close to that of the ideal gas.

System /Diffusivities	Translation (Absolute)	Translation (Relative)	Rotation (Absolute)	Rotation (Relative)	Interdigitation
A	2.36×10^{-5}	0.0052	2.0×10^{-5}	0.16	0.95
B	1.47×10^{-4}	0.066	1.95×10^{-5}	0.078	0.86
D	4.42×10^{-4}	0.0812	1.375×10^{-5}	0.11	0.50
C	9.7×10^{-4}	0.76	2.39×10^{-5}	0.17	1.17
A-50	5.35×10^{-5}	0.012	3.5×10^{-5}	0.24	Some cores touch
A-100	1.18×10^{-5}	0.0026	1.40×10^{-5}	0.11	0.76

Table 2.2. Effect of variation in corona on diffusivities for various systems

Table 2.2 lists the values of diffusivities and interdigitation for systems A, B, C and D. For system C the interdigitation is greater than 1, indicating that chains extend beyond the nearest neighboring cores due to the long tail of the corona thickness distribution (ξ). From the relative diffusivity we can clearly see that for pure PGNs, translational motion increases significantly as chain length increases (A< B < C) while rotational motion remains almost unchanged. This supports our earlier observation that when the chains become longer, the corona becomes more uniformly dispersed, caging of the

nanoparticles is reduced and translational diffusivity increases. The enhanced mixing of chains from neighboring particles with longer chains is also evident in the increasing values of interdigitation for systems B and C. The rotational diffusivity remains almost

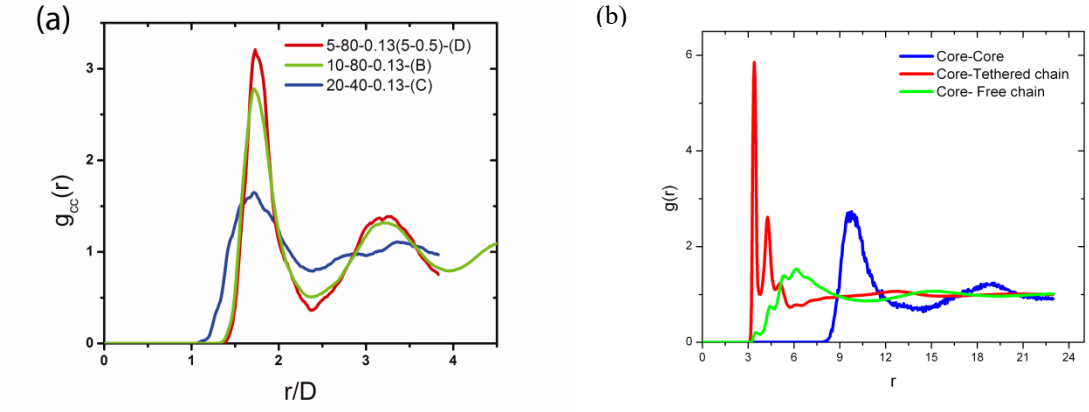

Figure 2.6. (a) Radial distribution function for system B, C, and D where ϕ_c=0.13 is fixed while chain length varies. (b) Distribution functions for cores, tethered, and free chains

constant in all cases and is unaffected by any change in corona, possibly because interdigitation values remain nearly constant resulting in a similar effective "friction" of a PGN with its surroundings. In Fig. 2.3(c), systems B and C are simply marked as liquids while system A is loosely marked as a "soft glass" due to the strong caging of its cores. Both translation and rotation diffusivities of the blend system D are slightly larger than those for system B but less than those of system C; this result and those for the equilibrium structure discussed before suggests that blends exhibit a more uniformly dispersed corona compared with a pure PGN system of the same grafting density and ϕ_c. This can be attributed to the extra mobility of free chains which allows the blend (D) to relax more readily.

We also studied the effect of changing GD with fixed N_m on the structure and mobility of pure PGNs. We used systems A-50, A, and A-100 where we have kept N_m=5

and changed GD from 50 to 100 (see Fig. 2.3(c) and Table 2.1). Table 2.2 and Fig. 2.7 give the simulated properties. We see in Figure. 2.7a that compared to system A, the thicker corona in the A-100 nanoparticles leads to a larger distance between neighbors and a taller first peak of g_{cc}(r). Effectively, the A-100 system experience stronger steric hindrance due to extra grafted chains making the net particle-particle interaction more repulsive and the lubricating corona less fluid-like. This causes resistance for interparticle motion and a reduction in translational and rotational diffusivity. For the system A-50, a thinner corona is observed along with a number of core pairs "kissing" at a distance of 6σ which is the diameter of the core. This arises as regions with fewer tethered chains or "bald spots" of two PGN surfaces come together experiencing a depletion-induced attraction (associated with the grafted chains). It should be noted that the grafting of chains at random points on the core surface is bound to produce some patchiness in the corona for lower GD; hence, the results for system A-50 will depend on the specific choices of chain anchoring points (though the effect is mild for relatively uniform spreading). Despite having a large ϕ_c (=0.32), the diffusivities for system A-50 are larger than those for systems A and A-100. This is explained by the decrease in the structural layering of the cores as ϕ_c increases; the presence of "kissing cores" in system A-50 seems to further contribute to the disordering of cores and to a more uniform distribution of chains (both of which reduce the caging of particles).

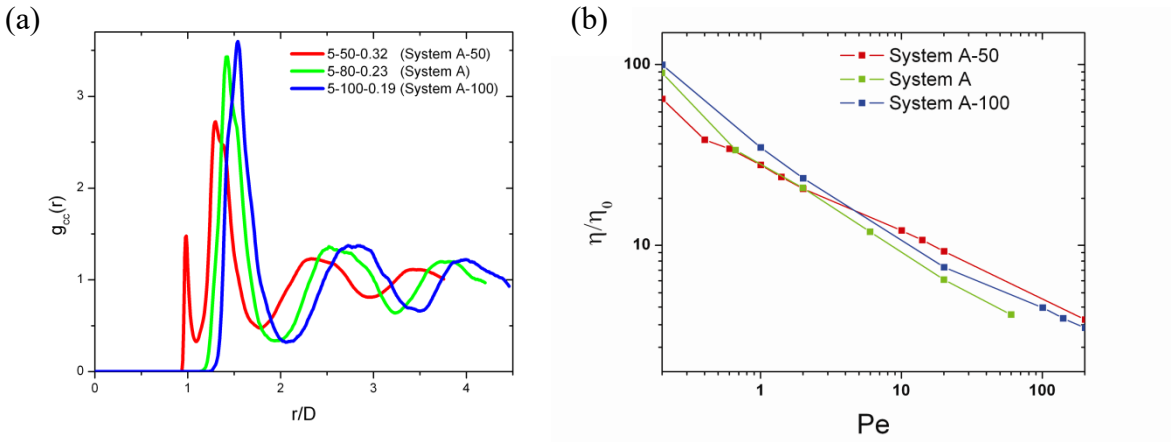

Figure 2.7. Properties of systems A, A-50, and A-100 (which only differ in GD and hence ϕ_c). a) Core-core radial distribution function; particles aggregate at lower GD due to bald core surfaces sticking together. (b) Viscosities as a function of Peclet number where a transition behavior occurs for system A-50 as large Pe induces the separation of "kissing" particles.

1.4.2 Viscosity and Yield Stress

To examine effect of GD on relative viscosities, we simulated the systems A-50 (5-50-0.32), A (5-80-0.23), and A-100 (5-100-0.19) under shear (see Fig. 2.7b). As noted earlier, the end-to-end distances of grafted chains increase with GD, seemingly increasing the effective friction between particles. This results in an increase of relative viscosities for system A-100 relative to system A (80% GD). For system A-50 (5-50-0.32) we observe the lowest viscosities for PE<6, likely because at low shear rates some particles stay aggregated (as in the equilibrium state) reducing the steric hindrance for the other particles and facilitating the overall flow. As Pe increases, the shear applied is enough to separate the particle aggregates and the viscosity becomes larger than that of the systems with lower ϕ_c.

System A-50 is marked as “aggregating fluid” in Fig. 2.3(c) as the tendency to form core-core contacts is the most distinctive characteristic. While all systems A are liquids based on their translational diffusivity behavior, systems A and A-100 are tentatively termed “soft glasses” in Fig. 2.3(c) to highlight their marked caged structure, relatively low translational diffusivity, and, as shown in the next Section, a large low-Pe viscosity (further evidence for system A-100 is given in Sec. 2.4.4). This classification is in approximate agreement with the trends observed in Ref. [12].

To study the effect of corona variation at fixed $\phi_c = 0.13$ on viscous response, we simulated the viscosities for systems B, C and D as shown in Fig. 2.8. Shear thinning behavior is observed for all cases. This behavior is consistent with experiments though we have not approached the range of Pe where Newtonian regime is observed for experiments.[2]

With increasing chain length at fixed $\phi_c = 0.13$, we observe a decrease in relative viscosity with system C always having lower viscosity than system B. Both pure systems follow power law behavior with an exponent of -0.4 while the blend system D has a lower exponent of -0.25. At high Pe all systems tend to have more similar relative viscosities due to chains being strongly aligned to the direction of flow (see Sec. 2.4.3). As this simulation method is not efficient to obtain low-Pe results, we also calculated the yield stress behavior. Figure 2.8 shows the stress versus shear rate curves for these systems along with the yield stress and yield strain. We observe that the pure systems require a finite stress to yield while the blend does not show a clear yielding behavior.

The region marked by the arrow shows the regime that was not accessed by our constant shear-rate simulations.

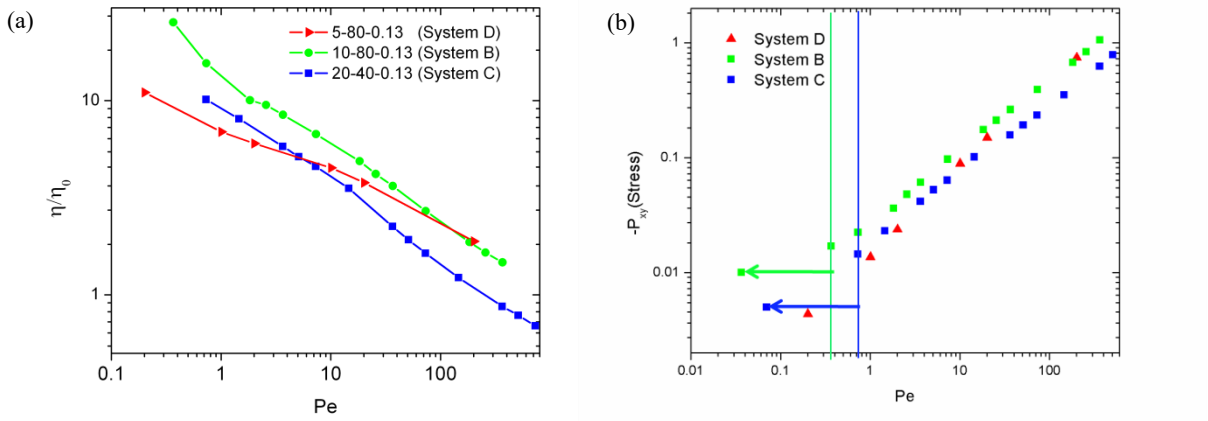

Figure 2.8. (a) Viscosity for systems A, B, and C as a function of Peclet number via constant shear-rate flow type simulation (b) Yield Stresses for systems A, B, and C via constant stress

1.4.3 Shear Thinning

1.4.3.1 Brownian Stresses

Figure 2.9 shows the relative viscous contribution due to Brownian stresses and relative viscosity as function of Peclet number. The Brownian stresses show a uniform shear thinning behavior similar to that of the total viscosities and can be considered as one of the contributors to shear thinning. Such an effect, however, is very small as evident from the ratio of Brownian contribution to total viscosity which is ~10^{-3} for the 1<Pe<1000. This occurs because Peclet numbers accessible to simulation are very large which by definition means a large ratio of convective to Brownian forces; hence Brownian forces are weak and have negligible effect on dynamics for Pe>>1.

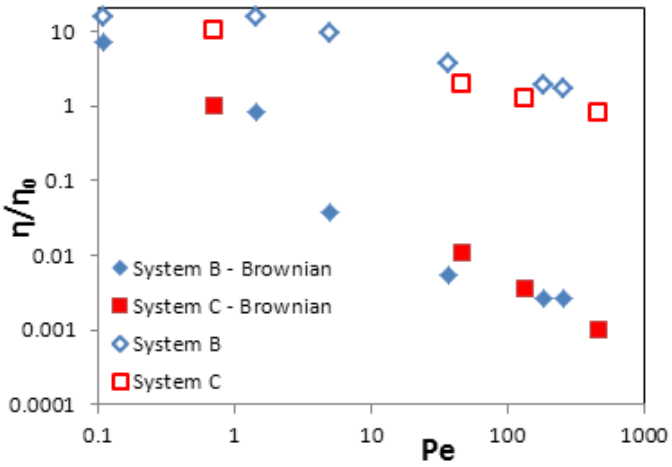

Figure 2.9. Comparison of actual viscosity and viscous contribution of Brownian stresses for systems B and C. Both systems shear thin but the relative contribution of Brownian stress is negligible at higher Pe.

4.3.2 Chain Alignment

We next examine results of the chain orientation function $f_{\theta'}$ (Fig. 2.10). Figure 2.10a plots $f_{\theta'}$ for increasing Pe: for Pe=0 (at equilibrium) there is no preferential chain alignment, for Pe=0.25 some alignment is evident while for Pe=50 chain alignment is very significant. Figure 2.10b shows $f_{\theta'}$ for systems A, B, and C at a fixed shear rate. We observe that longer chains align more easily than shorter chains. This partly explains why system C has lower viscosities than systems B and A. Figure 2.10c plots $f_{\theta'}$ for both grafted chains and free polymers in the blend system D at a fixed Pe of 10. We see that grafted chains align more than the free chains, which is likely due to the former having less freedom to reorient isotropically. Also shown in Fig. 10c, the free chains in the blend exhibit an extent of alignment which is intermediate between that of the grafted chain and that of the polymers in a melt (free of PGNs). Overall, these results

indicate that chain alignment is one of the causes for shear thinning, especially at high Pe numbers, and blends have a lower shear thinning slope because the free chains orient less in the direction of shear than grafted chains.

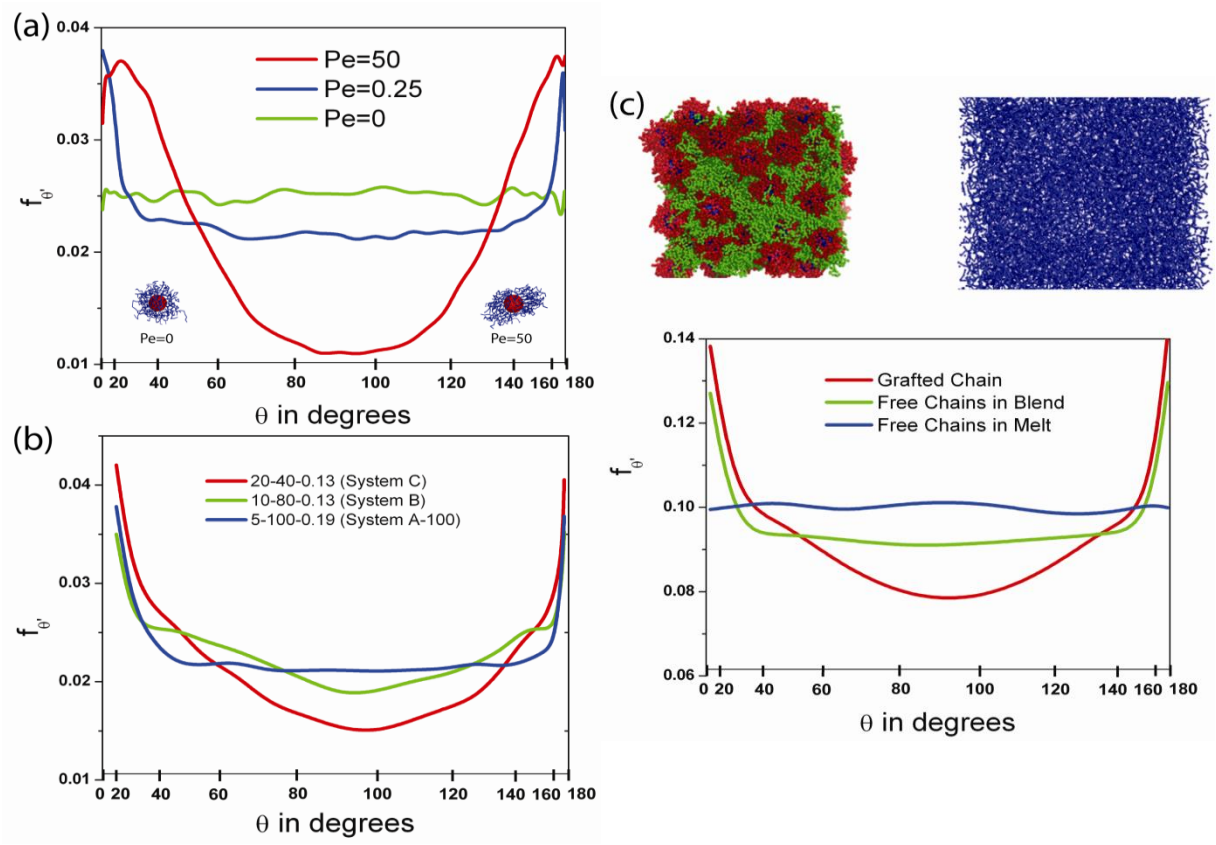

Figure 2.10. Chain orientation function $f_{\theta'}$ for various cases. Note the non-linear scale used for the x-axis to maintain a proper area normalization of $f_{\theta'}$. (a) Variation of $f_{\theta'}$ with Pe number for system B showing distortion of corona at high Pe. (b) Variation of $f_{\theta'}$ with chain length for a fixed shear rate ($\gamma\,\Delta t = 3.5\times10^{-6}$) showing more alignment for longer chains. (c) Variation of $f_{\theta'}$ for different types of chains in the blend system D and in a pure 5-mer melt (fixed Pe=10) showing that grafted chains (red curve) align the most. A snapshot shows the two systems with colors corresponding to $f_{\theta'}$ curves.

To elucidate the coupling between the spatial distribution of cores and the alignment of chains, we examined the existence of a "residual" chain alignment as described next. When the system is under shear, the equilibrium core-core distribution is altered to a non-equilibrium state (Fig. 2.11a) and polymers may have to orient anisotropically maintaining some of the shear-induced alignment to fill the space between nanoparticles (thus maximizing the chain conformational entropy). To quantify this residual chain alignment, we carry out the following steps, (1) starting with an equilibrium system, steady shear is applied until steady state is reached, (2) the position of all the core centers are frozen and the shear is turned off to only allow the chains to relax (cores are also allowed to rotate). Figure 2.11b shows the residual alignment of chains after shear has been turned off for system B. Figure 2.11c plots the residual alignment for various Pe numbers and we observe that it increases with Pe. We can then conjecture that shear thinning at these Pe numbers is due to a coupled effect of chain alignment arising from both the shear flow and a residual alignment associated with the non-equilibrium spatial distribution of cores.

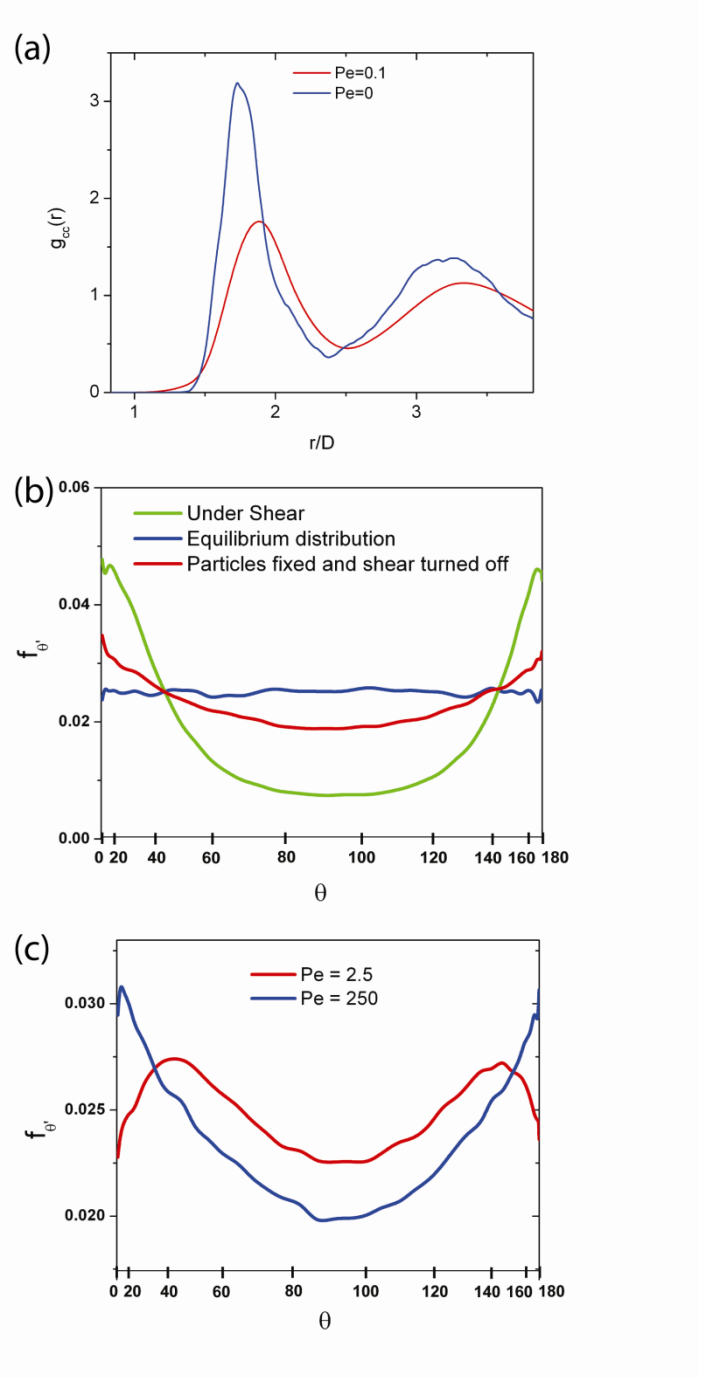

Figure 2.11. Effect of shear on system B. (a) Radial distribution function under equilibrium and at Pe=0.1 showing the perturbation in structure leading to residual chain alignment. (b) Residual chain alignment when system is equilibrated with cores held fixed at the Pe=0.1 structure. (c) Increase in residual chain alignment with Pe.

4.4 Uniaxial stretching and break-up.

We simulated the pure PGN systems A-100 and B-50 which possess the same core volume fraction (ϕ_c= 19%) but differ in grafted chain length. Representative results are shown in Fig. 2.12. As the box elongates and its volume increases, a large negative force (tension) along the z axis is generated (to sustain the deformation) while the system's density drops but remain uniform; this large tension eventually leads to defects that seed a very low density region (vacuum). The tension then starts to drop as the empty region grows and eventually vanishes as the dense (liquid) domain becomes fully separated by a "gas-like" interface. While the maximum in the tension vs. strain curve is similar (in height and location) for both systems, the post yield-point behavior is significantly different: the B-50 system (having the longer 10-mer grafted chains) forms a characteristic liquid bridge before a break-up that takes places at a much longer extension. In contrast, the A-100 system (with the shorter 5-mer chains) breaks-up earlier and more transversally with a minimal bridge; i.e., a behavior more reminiscent of that of a soft glass or solid. This liquid vs. glassy-like behavior agrees well with the difference in the core structure (shown in the inset of Fig. 2.12) where the B-50 has a much less structured and layered radial distribution than system A-100. These results are in line with the analysis of systems B and C (for a lower ϕ_c= 0.13) and the correlations between their diffusivities and structure described in section 2.4.1 and with their rheological behavior described in section 2.4.2.

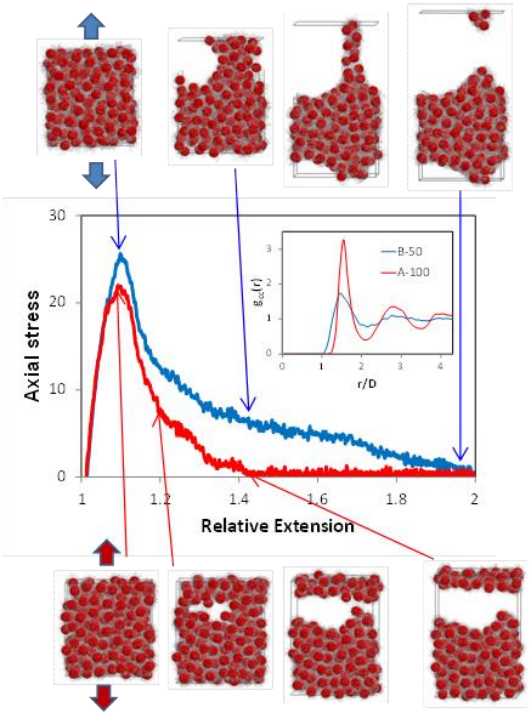

Figure 2.12. Constant cross-section uniaxial deformation of systems A-100 and B-50. The axial stress is the product of the instantaneous zz component of the stress tensor and the box z-length (in LJ units); the relative extension is with respect to the initial unperturbed box length.

5. Concluding remarks

In this work, we have studied the equilibrium behavior, diffusivities, and rheology of PGNs as self suspended colloidal systems for varying GD and N_m, while keeping fixed the core diameter. Comparing a system of pure PGNs with one in which a single PGN is infinitely diluted in an oligomer identical to the grafted chains, we found that the translational motion is greatly reduced due to the caging by neighboring PGNs, while rotational motion is only mildly reduced due to the lower mobility of the grafted oligomers. Depending on the combination of GD and N_m employed, pure PGNs exhibited distinctive fluid behavior that is qualitatively highlighted by different symbols

in Fig. 2.3(c). For combinations of GD and N_m that result in a fixed ϕ_c , we found that for shorter grafted chains the spatial distribution of cores becomes more structured (with better defined neighboring layers around a central core), the translational motion is reduced due to stronger caging by neighboring PGNs, and rotational motion is almost unaffected. Consistently, simulations of uniaxial stretching (also for fixed ϕ_c) show that systems with a longer chain length present a liquid-like break-up while the short chain system exhibits a soft-glass-like break-up. For fixed grafted chain length N_m, a reduction of GD (which also brings a corresponding increase in ϕ_c) leads to a non-trivial trend in core structure where for low enough GD some particle cores get in close contact (touching in areas of lowest GD) promoting faster translational and rotational diffusivities. Such close contacts also lead to low-GD systems to be less viscous than high-GD systems, a trend that is reversed as the shear rate is increased and the structure made more homogeneous.

Our constant-shear rate simulations revealed that all systems studied exhibit shear thinning behavior with the thinning exponent being greater for pure PGNs than for a blend system of equal ϕ_c. We found that systems exhibiting a more homogeneously dispersed corona have lower viscosities. Also, the introduction of free oligomer fluid to PGNs reduces the viscosity relative to pure PGNs of equivalent ϕ_c, at least in the range of shear rates we have simulated. The yield stress results are consistent with the stress-strain rate trends of the constant-shear rate simulations and also show that the blend system did not exhibit a clear yielding behavior. We also attempted to elucidate the microscopic origins of the observed shear-thinning behavior. We found that although

Brownian stresses decrease with shear rate, their viscous contribution is too small at the high Peclet numbers simulated to be a dominant driving force of shear thinning. When examining the extent of alignment of chains under shear, we find that systems with more uniformly dispersed corona tend to align more in direction of shear, giving a possible mechanism for the lower viscosity of PGNs with longer chains. We also found chain alignment to be more pronounced for grafted polymers than for free polymers which partly explain the flatter shear thinning slope of the PGN-polymer blend compared to pure PGN systems. Finally, we observed a residual chain alignment present in PGNs due to the shear-induced non-equilibrium distribution of cores, which must also affect the viscous response of the system.

An important question that arises is to what extent the properties of the PGN systems studied here could be described by using much coarser force fields; e.g., using a soft-sphere pair potential to represent the effective core-core potential of mean force. Indeed, our results that softening of the PGN corona (e.g., by grafting longer chains) leads to weakened core-core pair correlations and an increase in translational diffusivity have also been observed in simulations of Gaussian-core and Hertzian fluids.[31,32,33] Our more detailed PGN model, however, allows us to account for other effects that are associated with multibody intra- and inter-chain interactions, and with intrinsic or dynamic spatial anisotropies of the corona. For example, our model allowed us to probe rotational diffusivities, to find a connection between shear-thinning, chain alignment, and corona deformation, and to find depletion-driven close contacts between bald-spots of cores having low GD. Such effects could also be captured by a coarser-grained model than ours, e.g., one using fewer effective grafted chains that have fewer but larger beads

representing longer chain blobs (with softer interactions); more research would be needed to define such a minimalistic model.

This study is a first step toward understanding the physical behavior of the solvent-free PGNs of varying designs. In terms of thermodynamic behavior, it still unclear for example whether and how a liquid-to-solid transition ensues. In terms of rheological behavior, we were only able to probe Pe values as low as 0.1, while interesting experimental crossover behavior (to a Newtonian regime) of related systems is usually reached at much lower Pe values (~ 0.0001).[3] While constant shear-rate simulations for Pe ~ 0.001 could be attainable via very long simulations in massively parallel computing platforms, these may still be in the shear-thinning regime. Regarding our high-Pe shear thinning results, we note that the viscous contribution of chain alignment to stress could be further explored by calculating the pulling force applied by the chains on the nanoparticles. Also, our study has been confined to very small core sizes and monodispersed systems; polydispersity in particle size, chain length, and grafting density are non-negligible in experimental systems and can significantly affect the structural and rheological behavior. Lastly, nanoparticles of non-spherical shapes will likely result in a vastly different viscous behavior. Work on some of these extensions is currently under way

3 Effect of Curvature on Phase Behavior of Polymer Grafted Nanoparticles

3.1 Introduction

The dispersion of PGNs in solvent is characterized by the interpenetration of solvent chains into the grafted chains leading to stabilization of the suspension (wetting), or their expulsion causing nanoparticles to aggregate (dewetting). The solvent for the dispersion can be chemically identical or different from the grafted chains. Chemically different solvent allows for attractive interactions with grafted chains increasing the wetting behavior 55-60. Due to the absence of enthalpic driving forces, PGNs in chemically identical solvent form an interesting model system as the wetting/dewetting phenomenon is purely entropic in nature. For such PGNs, decreasing the ratio of solvent molecular weight to grafted chain molecular weight, increasing the number of chains attached to the nanoparticle(grafting density), and increasing the polydispersity in grafted polymer weight has been shown to favor the formation of a more stable dispersions8-12,39-51. A first approximation of PGNs as polymer brushes on flat surfaces has shown that the wetting behavior is directly related to the change in translation entropy of the solvent 61,62. When the solvent chain length is smaller than grafted chain length, solvent interpenetrates the grafted chains to maximize their translational entropy while for longer solvent chains, the gain in translational entropy for the solvent is countered by the decrease in entropy of the grafted chains due to swelling. Simulations have further shown that the dewetting behavior can be correlated

with a transition in the potential of mean force (PMF) between two approaching PGNs immersed in the solvent from repulsive to attractive 8,9,41.

Recent work has attempted to consolidate all the experimental data available on the phase behavior of PGNs dispersed in polymeric solvent onto a two dimensional diagram that uses a dimensionless grafting density and the ratio of solvent to grafted chain lengths as primary axes49,50. This phase diagram is shown in figure 3.1 where the black symbols represent the well mixed systems, red symbols the phase separated regions, and green the partially phase separated systems. The aforementioned theoretical results from polymer brushes grafted to flat surfaces (or "flat brushes") are shown in solid and dotted black lines. The figure illustrates that a number of well mixed systems are found to lie in the region where the theory for flat brushes predicts dewetted or aggregated system. This discrepancy has been attributed to the "curvature" of the nanoparticles which is defined in this text as the ratio of brush height of grafted polymer to nanoparticle size (flat brushes have zero curvature). Variation of curvature alters the distance between the grafting points on the surface and modifies the steric forces experienced by the grafted chains. This in turn affects the entropic interactions between the grafted chains and the free chains thus affecting the nanoparticle aggregation behavior. Hence, to understand the phase behavior of PGNs, it is important to take into account the curvature of PGNs.

Recent work has explored the effect of curvature on phase behavior using polymer mean field theory for two PGNs and suggested guidelines for calculating the interpenetration width between solvent chains and grafted polymers and its relation to phase behavior,

extending scaling arguments for flat surfaces to curved particles 69. It was also found that grafting density had a small impact on wetting behavior while curvature had a much more pronounced effect. PRISM theory8,9,39, density functional theory40 and molecular dynamics67 have been used to make predictions for the bulk behavior by calculating the PMF for two nanoparticles in solvent, outlining the effect of grafting density and solvent chain length on dispersion. Experiments and simulations 65 have recently studied the dispersion of polymer grafted nanorods in identical solvent and found gradual transition from wetted to dewetted state on varying the ratio of grafted chain length to solvent length. DPD simulations have also helped map out the phase diagram of such systems as a function of grafting density and chain length 64. Previous simulation studies of spherical PGNs in identical solvent have been restricted to one or two particles systems 10,57,67 which do not capture all multibody effects present in the bulk, therefore, in this study we focus our attention on effect of curvature on bulk PGNs.

Another notable feature of figure 3.1 is the lack of a distinct demarcation between phase separated systems and well mixed systems. Such a boundary could help extend theory for flat brushes to curved PGN's and help gain physical insights into these systems. One of the reasons for the absence of this boundary could be the presence of metastable states which are known to occur during phase changes. They have been shown to occur in multiple systems such as crystalline polymer system, liquid-solid crystalline system and diblock copolymers [73,74,75]. These metastable states are usually short lived but in some cases their stability can be observed over large timescales. Factors such as presence of polydispersity in chain length and particle size, impurities and various other imperfections can destabilize these metastable states and hence observing them is

difficult . However, experiments have been able to observe glassy behavior for self-suspended PGN's [76] which could be indicative of such metastable states. MD simulations are a convenient tool for the study the phase behavior of these systems due to great control over system parameters, which allows us to probe such regions more carefully. However, a key limitation of molecular dynamics studies (even those relying on coarse-grained models as ours) is that simulation time scales are many orders of magnitude shorter than experimental time scales and hence brute-force molecular dynamics alone will not be able to resolve the question of thermodynamic stability for states which are "long-lived" relative to simulation time scales.

In this work, we explore the phase behavior of densely grafted spherical PGNs in identical solvent as a function of curvature using molecular dynamics. For this purpose, we fix the grafting density and only vary the curvature by changing the relative sizes of the nanoparticle and the grafted polymer. Varying the preparation conditions, that is, the path in temperature and concentration space that the system follows until reaching the sought-after state conditions (i.e., room temperature and melt density), can favor the formation of either well-mixed or phase separated systems. When different outcomes were thus obtained, preliminary calculations suggest that these states (mixed and demixed) have very similar free-energies, and hence to have comparable stability (and possibly coexist). The preparation protocol that we followed (to be detailed in section 3.2.3) tended to favor phase separated states (noting that some systems become fully mixed regardless of preparation protocol). As PGNs are sluggish systems with relatively long relaxation times, we run our simulations for a long time to verify the relative "stability" of observed phase separated states, at least over simulation time scales.

Following protocols that favor mixed states and fully characterizing them is an important complementary task that will be the object of future investigations but it is beyond the scope of this work; we focus here on preparation conditions that favor phase separated systems and on characterizing the resulting phases.

Since in our systems the grafted and free chains have identical size (P/N=1) and the grafting density is fixed to a high value (which translates into a range of dimensionless grafted densities), they can be mapped onto the shaded blue region in figure 3.1. It should be noted that correlating grafting densities between experiments and simulations is difficult owing to the coarse grained nature of the simulated polymers (e.g., the relative thickness of a model chain is larger than that of real chain). A more detailed explanation for the bounds of the blue region can be found in the methods section of this paper. For the range of high dimensionless grafting densities probed by our simulations (i.e., the blue region of figure 3.1), all experimental systems exhibit a single-phase, well-mixed behavior. In contrast, we find that on increasing the curvature of the PGNs, our simulated systems displayed both well mixed states as well as a metastable two-phase states (referred to as phase separated) with a corona-rich phase and a solvent-rich phase. This discrepancy is conjectured to arise from two potential sources: (i) Subtle entropic effects associated with molecular details of the system that would not be completely captured by the two axes in Figure 3.1, and (ii) the (slight) metastable character of the simulated phase-separated states. These results allowed us to assemble a tentative phase diagram outlining the conditions where well-mixed and phase-separated regions occur.

The rest of the paper is structured as follows. In Sec. II, we describe the simulation model, the method for creating bulk structures, and the methods for analysis. In Sec. III, we present the results for bulk systems and elucidate the effect of curvature on phase behavior, including the phase diagram for PGNs in chemically identical solvent. In Sec. III we conclude by providing some closing remarks.

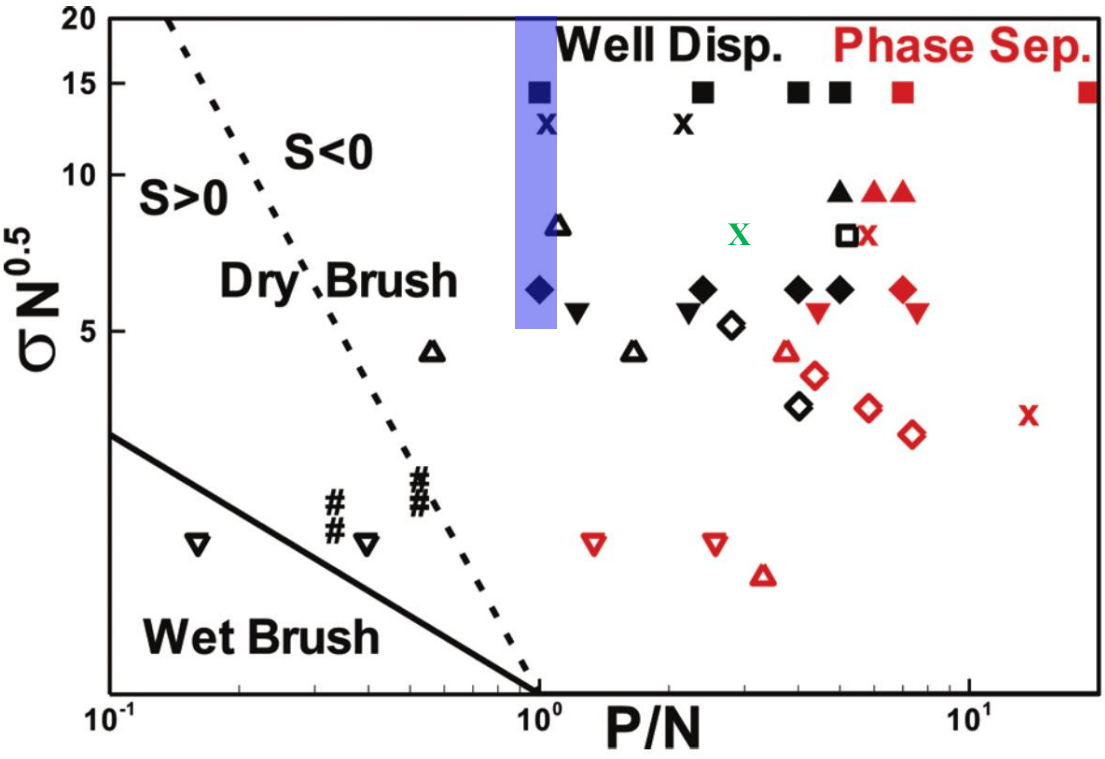

Figure 3.1 The experimental phase diagram identifying the mixing state of PGNs with identical polymer solvent for different combinations of grafting density σ and the ratio of solvent(P) to grafted chain lengths(N) from various experimental reports. Black symbols representing well mixed states, red symbols are phase separated states, and green denoting partial phase separation. S is the spreading coefficient and the regions given by S<0 is the theoretical limit for flat surfaces where they completely phase separate. The blue rectangle

roughly represents the region explored by our simulations. Various symbol types represent different sources details of which can be found in reference 29 which is the source of the figure (adapted from S. Srivastava, P. Agarwal, L.A. Archer, Langmuir. 28, 6276 (2012))

3.2 Method

3.2.1 Nanoparticle Model and Interactions

Due to its open-source massively parallel implementation, we use LAMMPS to perform MD simulations [68]. The nanoparticles are modeled as spheres of radius R_n. To create tether points on the surface of the nanoparticles, stiff springs are attached between a center particle and the required number of "surface particles" with a diameter *D*. The numbers of such surface particles are chosen to tessellate the surface of sphere with radius R_n. The equilibrium length of the stiff spring between the center particle and surface particles is used to set the radius of the nanoparticle. These surface particles repeal each other with Weeks-Chandler-Anderson (WCA) potential and their packing on the spherical surface is found by minimizing the energy of this system using the steepest descent algorithm. The position of surface beads are used as grafting points for the polymers to obtain PGNs of high grafting density (GD) where $GD = \frac{Number\ of\ chains\ attached}{Number\ of\ surface\ beads} \times 100$,in this work we use a uniform grafting density of 100 which corresponds to the densest grafting in this model. To compare this grafting density to experiments, 100% grafting density corresponds to ~1.2 chains per nm^2 . The

grafted chains have a molecular mass of 25-100 kg mol^{-1} and gives us a range of 5 to 25 for $\sigma N^{0.5}$.

Finally, the center particle and surface beads are frozen to form a rigid body with no relative motion. Note that once their positions have been set, the surface particles act purely as tether points and do not have any interaction except for the rigid body constraints with respect to the center of the nanoparticle. This is shown pictorially in figure 3.2.

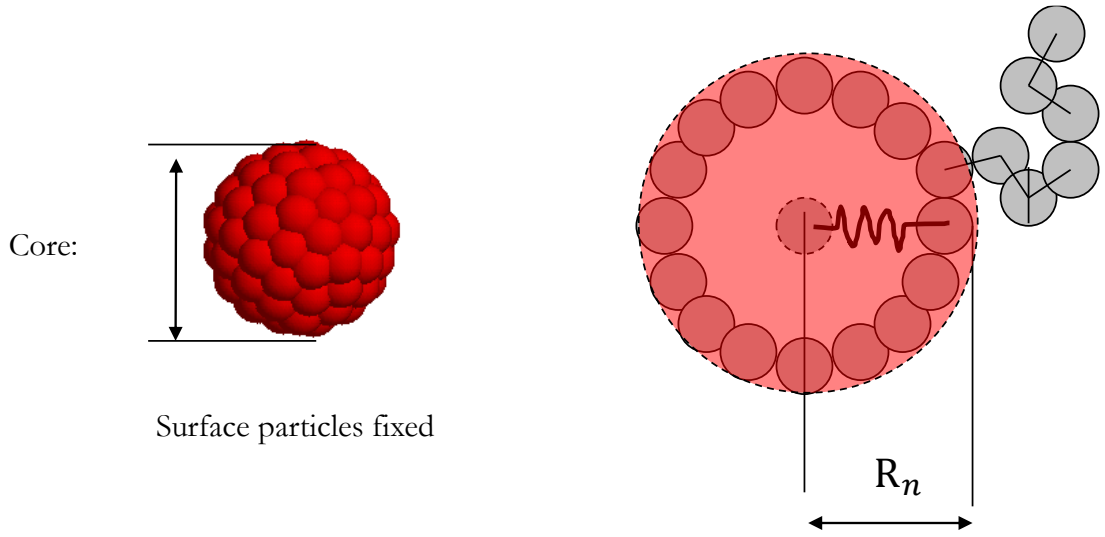

Figure 3.2 Schematics of (a) the surface of the tessellated surface of the nanoparticle for high grafting density, (b) model used to create nanoparticle of radius R_n by attaching surface beads to a central bead with stiff springs.

To model the non-bonded interparticle interactions, we use the expanded Lennard-Jones (LJ) potential which has the form $U_{ij} = \begin{cases} 4\epsilon_{ij}\left[\left(\frac{\sigma_{ij}}{(r_{ij}-\Delta_{ij})^2}\right)^{12} - \left(\frac{\sigma_{ij}}{(r_{ij}-\Delta_{ij})^2}\right)^{6}\right] & r < r_{cut} \\ 0 & r > r_{cut} \end{cases}$

with a cutoff of $r_{cut} = \Delta_{ij} + \Delta_{pair}$,

where ϵ is the energy of interaction, σ is the polymer bead diameter, and Δ_{ij} is the shifting distance which accounts for excluded volume by ensuring $U_{ij} = 0$ when particles are in contact. Δ_{ij} is given by $\frac{\Delta_i+\Delta_j-1}{2}$ where Δ_{i} is the diameter D_n for nanoparticles, and σ for polymer beads. The solvent chains are identical to the grafted chains in length and interactions parameters. ϵ for nanoparticle-polymer, nanoparticle-nanoparticle and polymer-polymer is 1.0. Δ_{pair} is used to switch between the LJ and WCA potentials; for nanoparticle – polymer and polymer-polymer $\Delta_{pair} = 2.5$ which allows for attractive and repulsive parts of the potential, while for nanoparticle-nanoparticle it has a value of $\Delta_{pair} = 2^{\frac{1}{6}}$ which gives a purely repulsive potential. The potentials were cut and shifted to have a zero value at r_{cut}. Figure 3.3 illustrates the potential for the interparticle interactions.

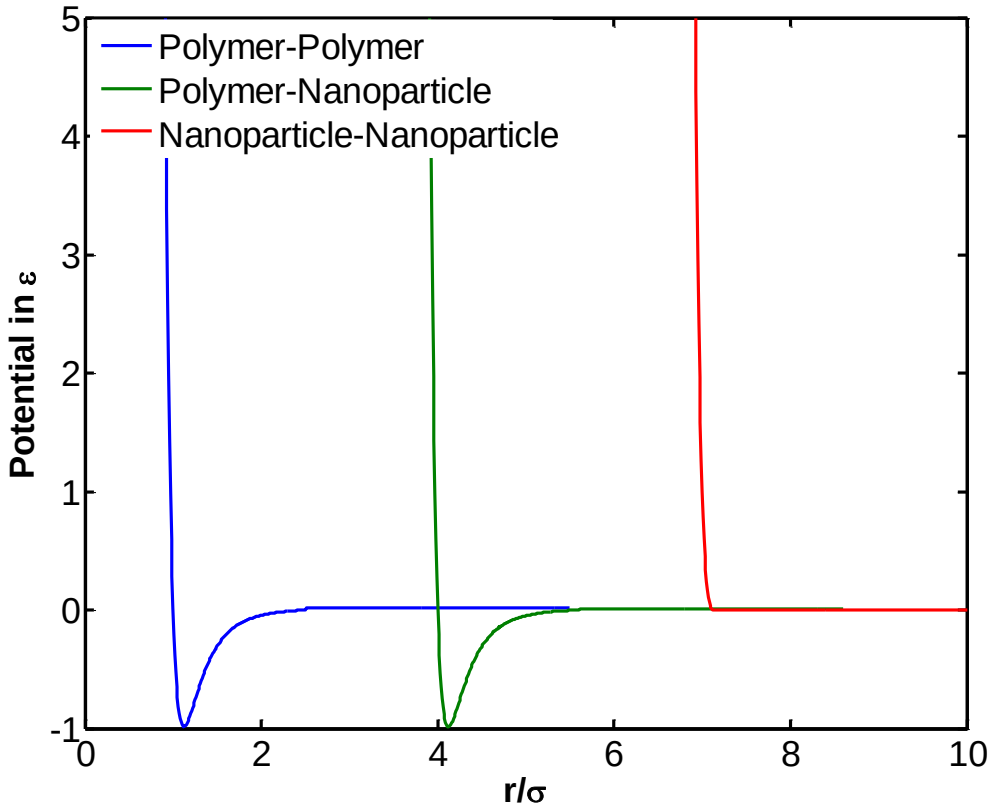

Figure 3.3 Inter-particle interaction potentials between the nanoparticle-nanoparticle, nanoparticle-polymer and polymer-polymer.

Linear polymers of length N_m are formed by joining bonded monomer beads by a harmonic springs with the potential given by

$U_{spring} = k(x_1 - x_{eq})^2$ with $k = \frac{2500\epsilon}{\sigma^2}$.

No bending or torsional angle potentials are considered in our model polymer chains, consistent with a level of coarse graining wherein one bead approximately corresponds to a Kuhn length along the backbone of the actual polymer.

3.2.2 Curvature of PGNs

We define the curvature of the PGNs as $\zeta = \frac{R_g}{R_n}$ where $R_g$is the radius of gyration of the grafted polymer for solvated systems (which was approximately constant for the range of dilutions simulated). R_g Is calculated using the formula $R_g^2 = \frac{1}{N_m} < \sum_{k=1}^{N_m}(r_k - r_{mean})^2 >$ where r_k is the position of k^{th} bead in the polymer chain and r_{mean} is the mean position of the polymer chain is given by $r_{mean} = \frac{1}{N_m}(\sum_{k=1}^{N_m} r_k)$. To study the effect of the amount of solvent, we vary the fraction $\phi_s = \frac{number\ of\ solvent\ chains}{number\ of\ grafted\ chains}$ which varies from $\phi_s = 0$ for solvent-free PGNs to $\phi_s \to \infty$ for an infinitely dilute PGN. Varying ϕ_S will also vary the core volume fraction ϕ_c given by $\phi_c = \frac{(number\ of\ cores)\times\frac{\pi}{6}D_n^3}{Volume\ of\ simulations\ box}$. The corona thickness,$\xi$, is calculated as the distance from the surface of the nanoparticle at which 90% of the grafted chain beads are found. This is explained in more detail in a previous paper [70]. To mimic oligomeric behavior via freely jointed chains, the minimum length of our polymers is restricted to 5 LJ beads

3.2.3 Generating the System and Other Simulation Details

We generate systems by two different methods, in the first method we observe both well mixed and phase separated system while in the second always well mixed systems are observed. The difference in the two methods lies in the initial volume and the procedure used to create the system and are described subsequently. In the first method, we performed simulations at $T^* = 1.0$ and $P^* = 0.1$, where T^* and P^* are the reduced

temperature and pressure (in LJ units). We place grafted nanoparticles and solvent randomly in the simulation box slightly larger than the equilibrium box volume (~ 2 times). To prepare the system for our simulations, we first relaxed the system using energy minimization via the steepest descent method. We next performed isothermal-isobaric ensemble (NPT) simulations using the Berendsen barostat and the DPD thermostat [71] with a pressure damping constant of 10 t^* where t^* is the non-dimensional time given by $t^* = \left(\frac{m\sigma^2}{\epsilon}\right)^{0.5}$. This was followed by production runs in the canonical (NVT) ensemble using the DPD thermostat. The simulations were performed with a time step of $0.005t^*$ and were run for 10τ for the NPT pre-equilibration runs and up to 1000τ for the NVT production runs. τ here is the structural relaxation time which roughly correlates to the time taken by the nanoparticle to diffuse a distance equal to its diameter and is given by $\tau = \frac{R_n^2}{Diffusivity} \sim \frac{6\pi\eta R_n^3}{k_B T}$ where η is the zero shear viscosity of the polymer solvent in the pure melt state.

In the second preparation method, we start with a simulation box significantly larger than the equilibrium box size (~20 times). Grafted nanoparticles and solvent is randomly placed in the box and steepest descent method is used to partially equilibrate the system. We then perform NPT simulation at P^*=0.1 and reduce the temperature from T^*=4.0 to T^*=1.0 in steps of ΔT^*=0.2. This simulation is run for 75τ time and is followed by NVT simulation for up to 1000τ for production runs. Berendsen barostat and DPD thermostat are used for these simulations and the details are same as the first method.

When these two preparation protocols led to states with different states of mixing, preliminary simulations showed that the difference in free energy between the phase-segregated and fully-mixed systems was of order $0.1k_BT$, making it difficult to determine with certainty which state is more stable (though the mixed system would have the slightly lower free energy). We also find that both states are stable for our simulation time scales and resistant to thermal annealing for up to temperatures of 3.0. Systems created from the second method will be the subject of a future study and all systems studied in this work were created using the first method.

The equations of motion were integrated using the velocity Verlet algorithm. All the systems consisted of 256 nanoparticles and specific characteristics of the PGNs simulated are provided in table 3.1. We initially fix the diameter of the nanoparticle and vary the chain length of the polymer but to obtain lower curvatures, we vary the particle diameter as well so that the grafted chain length is never less than 5 beads. Each PGN type will be identified by its curvature, and any system (PGNs + free polymer) will be denoted by using the convention "curvature:ϕ_s" to also specify the degree of dilution (e.g., system 1.04:1 contains PGNs with curvature 1.04 and one solvent chain per grafted chain

Curvature	Diameter of nanoparticle D_n in σ units	Chain length of polymer N_m in σ units	Number of Grafting Points	Box Size in σ units for solventless system
1.29	6	15	80	73.78
1.05	6	10	80	65.22
0.75	6	8	80	61.06
0.70	6	5	80	53.50
0.58	8	8	140	74.42
0.50	8	5	140	65.77
0.35	10	7	220	84.92

Table 3.1. Simulation parameters of the various systems studied.

3.3 Results

To understand the effect of curvature on bulk structure, we start our analysis by choosing two extreme curvatures. For each of these curvatures, we simulate a range of ϕ_c by changing the amount of solvent (ϕ_s) while keeping R_n and N_m constant. Our analysis starts with the simulation of solvent-free PGNs which have the highest ϕ_c, followed by increasing the solvent content to study effect of dilution on the microstructure. The two PGNs chosen are the small-curvature system with $\zeta = 0.35$ ($N_m = 7\sigma$ and $D_n = 10\sigma$), and the large-curvature system with $\zeta = 1.04$ ($N_m = 10\sigma$ and $D_n = 6\sigma$).

3.3.1 Low Curvatures

We first report on the small curvature system $\zeta = 0.35$. The solvent-free PGN system (ϕ_s = 0) has a volume fraction of $\phi_c = 0.25$ while the most dilute system studied has a $\phi_c = 0.10$ (ϕ_s= 2). By visual inspection of various sections of the structure of these systems, we find that the particles are uniformly dispersed and hence can be regarded as well mixed, with no hint of phase separation for all ϕ_s values tested. Figure 3.4(a) shows the equilibrium snapshot of the system while Figure 3.4(b) plots the core-core radial distribution function for these systems. The location of the first peak of g(r) signifies the most probable distance of pairs of nearest neighbor nanoparticles and its height is correlated to the probability of that separation. We observe that on dilution, the first-peak height of g(r) increases from $\phi_c = 0.25$ to $\phi_c = 0.20$, followed by a decrease from $\phi_c = 0.20$ to $\phi_c = 0.10$. To understand this trend we calculate the corona thickness of the grafted chains; for the solvent-free system we find that $\xi = 3.3\ \sigma$

while for all solvated systems $\xi = 3.6 \pm 0.3\,\sigma$. This result implies that on adding solvent, the grafted chains swell slightly. As the grafted chains are short and densely grafted, the PGNs could be conjectured to approach the behavior of hard spheres of an effective diameter $D_{eff} = D_n + 2\xi$. On starting with a dilute system, as the concentration of the nanoparticles increases, the g(r) peak initially increases, owing to the increasing short-range structural correlations in the system, which are maximized for $\phi_c = 0.20$. For hard sphere systems, increasing core volume fraction further would continue to increase the peak of g(r) but as PGNs are soft colloids, the corona thickness reduces from 3.6 to 3.3 allowing for a more dispersed system which leads to a reduction in peak of g(r). These results are consistent with recent experiments where the first peak of the structure factor was found to follow a similar trend [72].

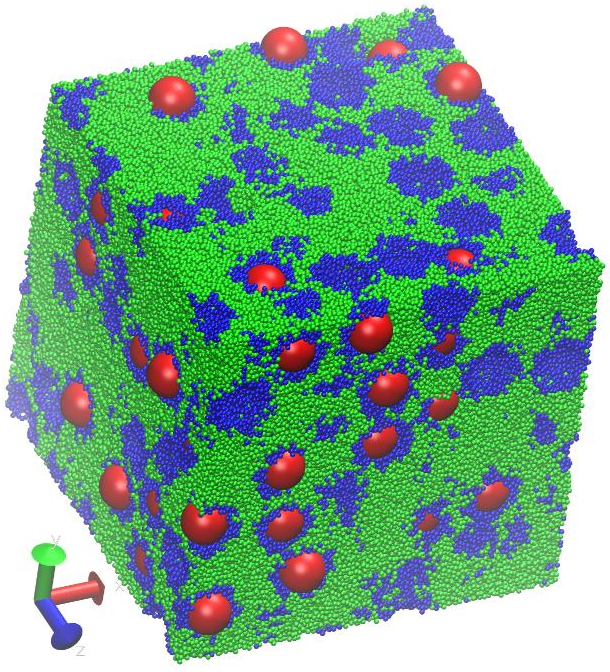

Figure 3.4(a) Snapshot of well mixed system with with (ζ, ϕ_s) = 0.35:1.Nanoparticles cores are red, grafted polymer beads are blue and solvent polymer beads are green. Note that nanoparticle centers are shown as spheres of size 6σ and hence those that cross the periodic boundary appear as naked when they are actually completely grafted.

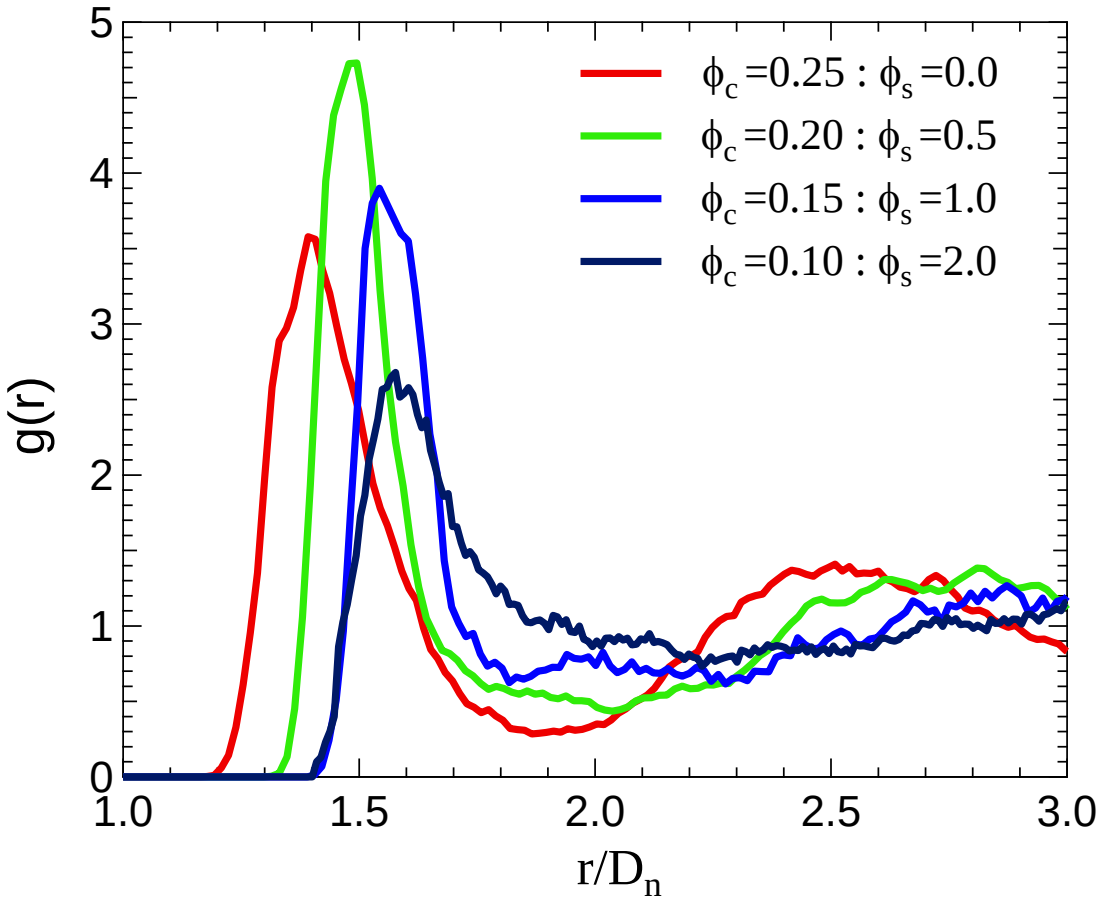

Figure 3.4 (b) Core-core radial distribution function for PGNs with curvature $\zeta = 0.35$ for varying nanoparticle concentrations.

3.2.2 High Curvatures

We next study the large curvature PGN with $\zeta = \frac{R_g}{R_n} = 1.04, D = 6\sigma$ and $N_m = 10\sigma$. The self-suspended PGNs have a $\phi_c = 0.127$ (for ϕ_s = 0) which decreases to $\phi_c = 0.04$ on dilution (for ϕ_s = 2). Visual inspection of selected views of snapshots of systems with $\phi_s = 0.5, 0.75, 1.0$ and 2.0 reveal clear evidence of phase separation; the system phase separates into two distinct spatial domains: a *PGN rich or corona rich* domain, and a *solvent rich* domain. Figure 3.5(a) illustrates snapshots depicting the bulk system, and the nanoparticles with corona for $\phi_s = 1$. Figure 3.5(b) plots the core-core radial distribution function for these systems.

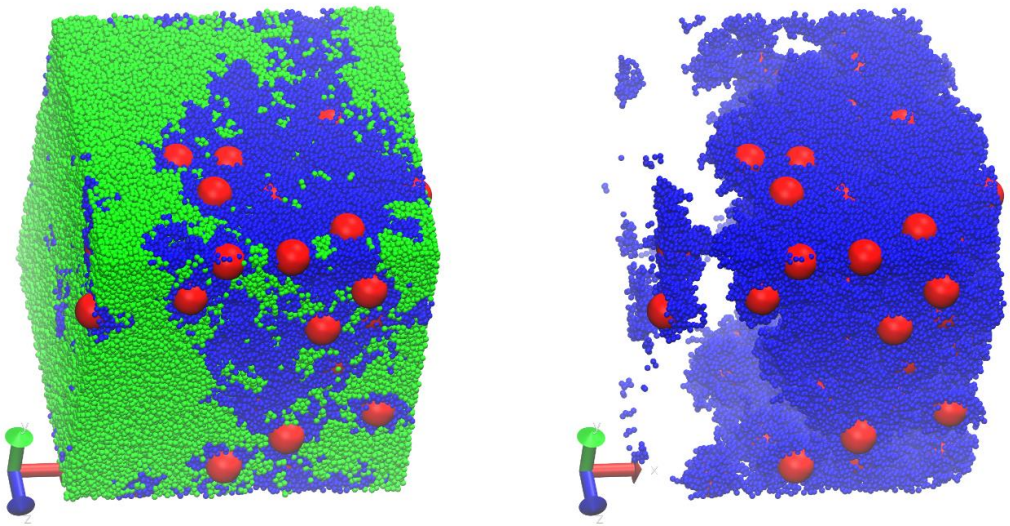

Figure 3.5(a). Snapshots of phase separated system with (ζ,Φ_s) = (1.04:1). The figure on the left shows the nanoparticle cores and all chain beads in the system while the figure on the right only shows the cores and grafted corona beads.

Nanoparticles are shown in red, grafted polymer beads in blue, and solvent beads in green. Note that nanoparticle centers are shown as spheres of size 6σ and hence those that cross the periodic boundary appear as naked when they are actually completely grafted.

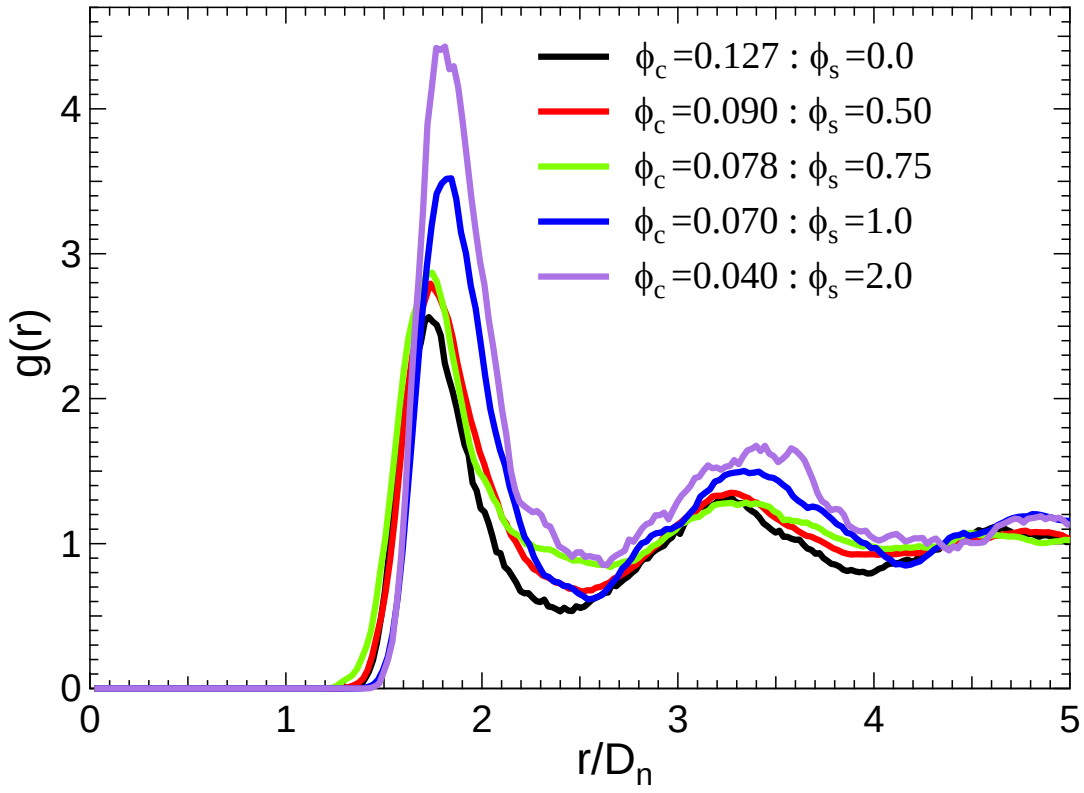

Figure 3.5(b) Core-core radial distribution functions for PGNs with curvature of $\zeta = 1.04$ as a function of nanoparticle concentration.

We observe that the height of the first peak of the radial distribution function increases monotonically on dilution. This trend is inconsistent with the expected behavior of

dispersed colloids for which on dilution, the distance between particles increases and spatial correlations decrease, lowering the g(r) peak heights.

3.3.3 Effect of Polydispersity

A possible driving force for the phase separation could be the depletion forces associated with excluded volume interactions of the nanoparticles and the solvent which results in a net attraction between nanoparticles. Recent simulations have shown that on increasing the polydispersity in grafted chain length, depletion forces vanish for large polydispersity of 2.5. Hence, to reduce the effect of depletion forces, we perform simulations for PGNs with increasing chain polydispersity. A Log normal distribution is used to assign lengths for grafted chains and the standard deviation of the distribution is used to quantify the polydispersity. In this study, all the PGNs were identical in terms of chain-length distribution. Figure 3.6(a) shows the effect of polydispersity on solvent-free PGNs. We find that on increasing the chains polydispersity, the microstructure becomes more homogeneous as evidenced by a reduction in the peak heights and valley depths. We perform the same simulations for PGNs with added polymer solvent (ϕ_s=1) and the results are shown in figure 3.6(b). We observe that even with a large polydispersity of 2.5, there is no change in the observed radial distribution function or the phases observed visually. This suggests that depletion forces do not cause the phase segregation.

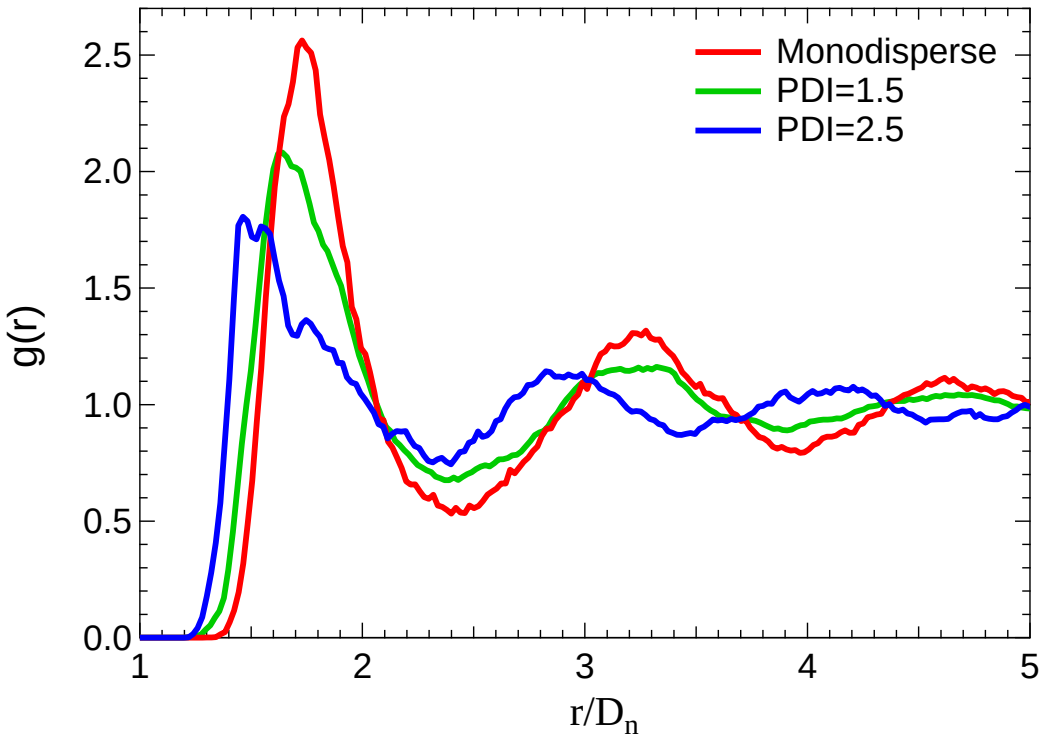

Figure 3.6(a) Core-core radial distribution functions for self-suspended PGNs with curvature of $\zeta = 1.04$ and varying degrees of grafted chain length polydispersity (PDI).

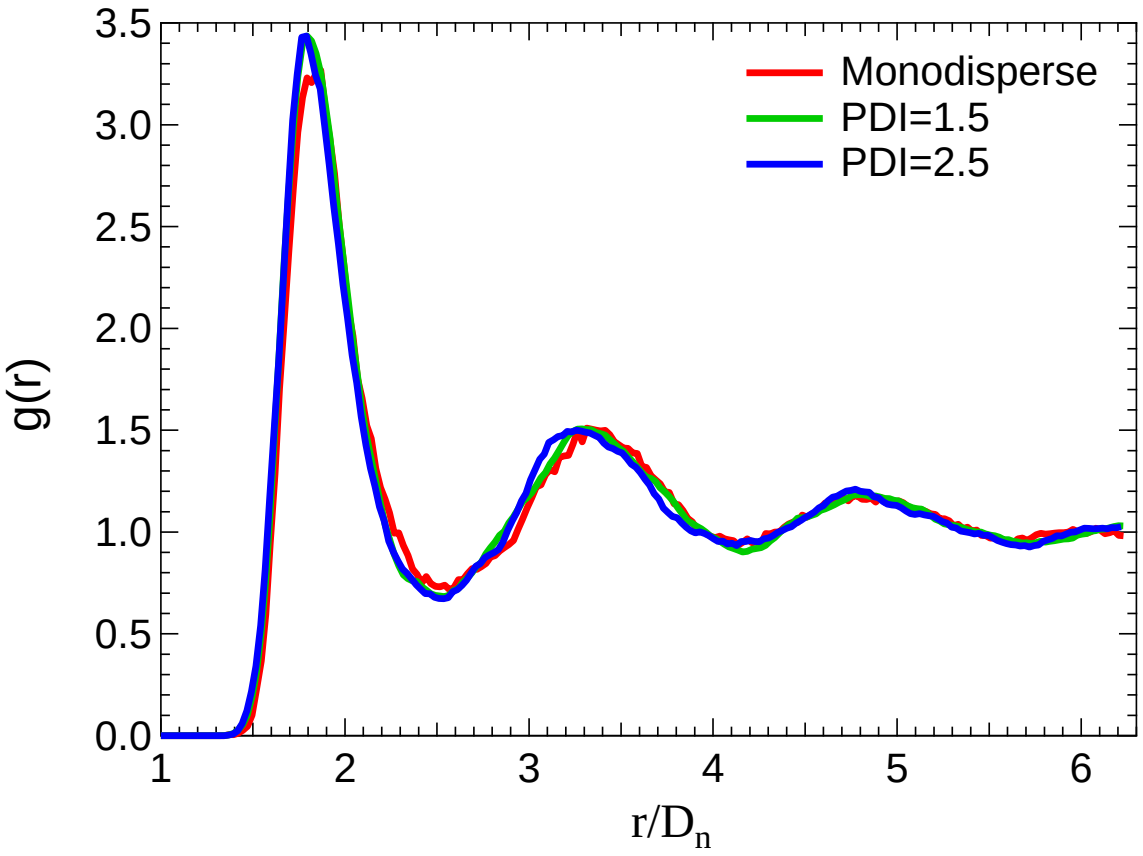

Figure 3.6(b) Core-core radial distribution functions for PGNs with curvature of $\zeta = 1.04$ and $\phi_s = 1.0$ with grafted chain lengths of varying degree of polydispersity.

3.3.4 Diffusivity

To investigate the phase behavior further, we study the mean squared displacement (MSD) for PGNs with fixed curvature and varying solvent content. Diffusivity is defined as $D^* = \frac{1}{6}\lim_{\Delta t\to\infty} < r^2(\Delta t) > \times \frac{1}{D_{SE}}$, D_{SE} is the Stoke-Einstein diffusivity given by $D_{SE} = \frac{k_B T}{6\pi\eta R_n}$ where η is the zero shear viscosity of the solvent. For a phase separated

system with diffusivity D_{P1} for phase 1 and D_{P2} for phase 2, addition of solvent will change the relative amount of the phases of each system and hence the diffusivity of the system can be given by $D = \theta_{P1}D_{P1} + \theta_{P2}D_{P2}$ where θ_{P1} and θ_{P2} are amount of phase P1 and P2. This is in contrast to the case of well-mixed systems, for which the addition of solvent will uniformly increase the average interparticle distances, hence increasing the diffusivity. Figure 3.7 shows the MSD plots for systems 1.04:0, 1.04:0.5, and 1.04:1, where we observe that self-suspended PGNs have a diffusivity of $D^* = 0.082$ which is different than that for the two solvated PGNs which have the same diffusivity of $D^* = 0.17$, this result is consistent with a phase separation scenario where one of the phase is in larger amount than the other.

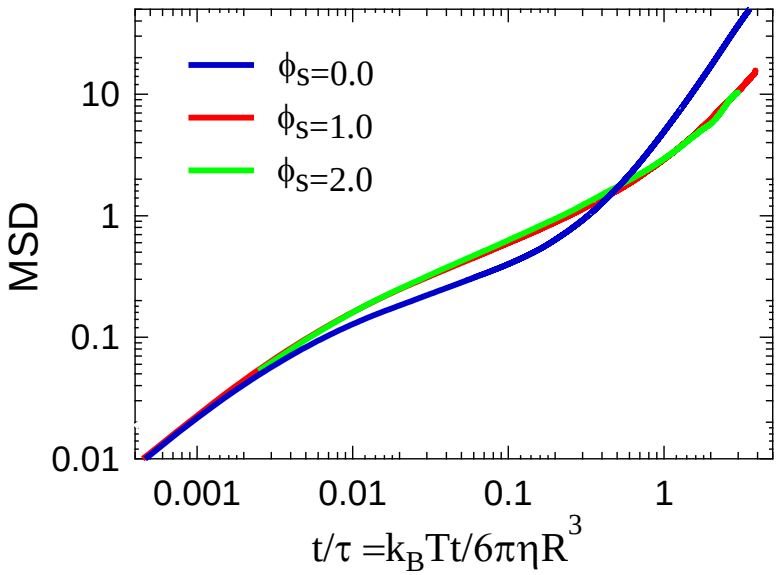

Figure 3.7 Mean squared displacement for systems with $\zeta = 1.04$ and varying solvent content. On dilution the diffusivity decreases and does not change on further dilution.

3.3.5 Density Distribution for Polymers

To estimate the amount of solvent-rich phase and corona-rich phase, we analyze the density distribution in the system. We construct a normalized histogram of frequency of observing density difference ($\Delta\rho$) between the grafted chains and free chains. To calculate these histograms, we divided the system into voxels of size $2\sigma \times 2\sigma \times 2\sigma$ and counted the number of grafted and free polymer beads in each such voxel; the density difference was then calculated by $\Delta\rho = \frac{\#grafted\ beads - \#free\ beads}{8\sigma^3 - V_{int}}$, where V_{int} is the intersection volume between any nanoparticle core and the cubic voxel.

Figure 3.8 plots the density distribution for the system $\zeta = 0.70$ with $\phi_s = 0.50$ and 1.0 with two calibration curves to illustrate the density distribution for pure solvent and solvent-free PGNs. The calibration curves show that the pure solvent presents a peak at $\Delta\rho \sim -0.8$, while solvent-free PGNs exhibit a peak at $\Delta\rho \sim 0.80$. The system $0.70{:}\,0.5$ is a well mixed system and does not show a solvent or corona rich region; on addition of solvent, the resulting $0.70{:}\,1.0$ system shows two distinct peaks for the solvent rich or corona rich region. This result illustrates that for medium curvature systems, addition of solvent can cause a well-mixed system to phase separate. Figure 3.9 shows a plot of the $\Delta\rho$ distribution for systems with high curvature, namely, for 1.04:1 and 1.04:0.5. Here we observe two distinct peaks which are more pronounced than those in well mixed system of Figure 3.8. We also observe that on dilution, the peak height increases for the solvent-rich phase while it decreases for the corona-rich phase. This suggests

that on addition of solvent, the system separates into the same two phases but with different amounts (which correlates with the change in peaks heights). We will use these $\Delta\rho$ plots to estimate the net amount of each phase by assigning the solvent-rich phase to correspond to the area under curve for $\Delta\rho < 0$, and the corona-rich phase to correspond to the integral for $\Delta\rho > 0$.

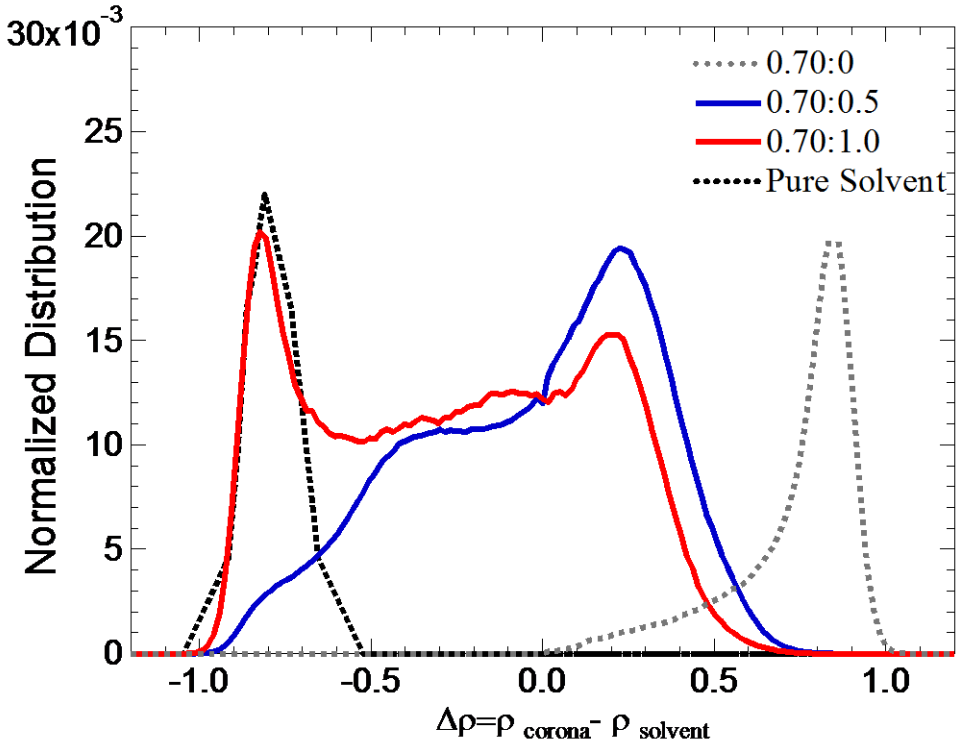

Figure 3.8. Weighted histogram plot for systems with low solvent (0.7: 0.5, full blue line) and high solvent content (0.7: 1.0, full red line). Two distinct peaks at Dr = 0.25 and -0.85 appear upon addition of solvent suggesting phase separation. Dotted lines correspond to the distributions for the pure solvent (leftmost curve) and solvent-free PGNs (rightmost curve)

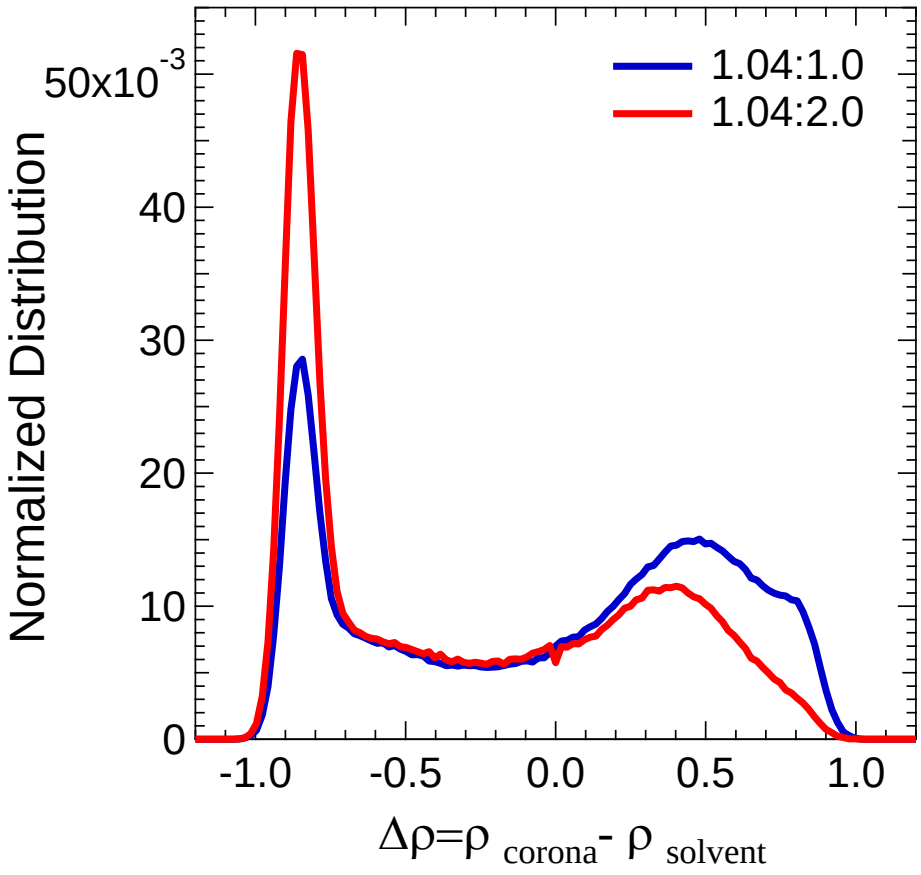

Figure 3.9. Normalized histogram for system 1.04: 1 and 1.04: 2. We observe that the location of the peaks remain the same while their relative heights change.

To confirm the occurrence of phase separation, we compute the radial distribution function of the nanoparticles that lie in the corona rich phase only and compare it to the bulk result. For calculating the core-core g(r) for the corona-rich phase, we use the formulae $g(r) = \frac{Number\ of\ Nanoparticles\ within\ distance\ r}{Number\ of\ ideal\ gas\ particles\ at\ distance\ r}$ for the voxels where $\Delta\rho \geq 0$ corresponding to the corona-rich phase. Figure 3.10 plots the first peak of the corona-rich phase g(r) [recall that Figure 3.5 showed the bulk g(r) for the entire system].

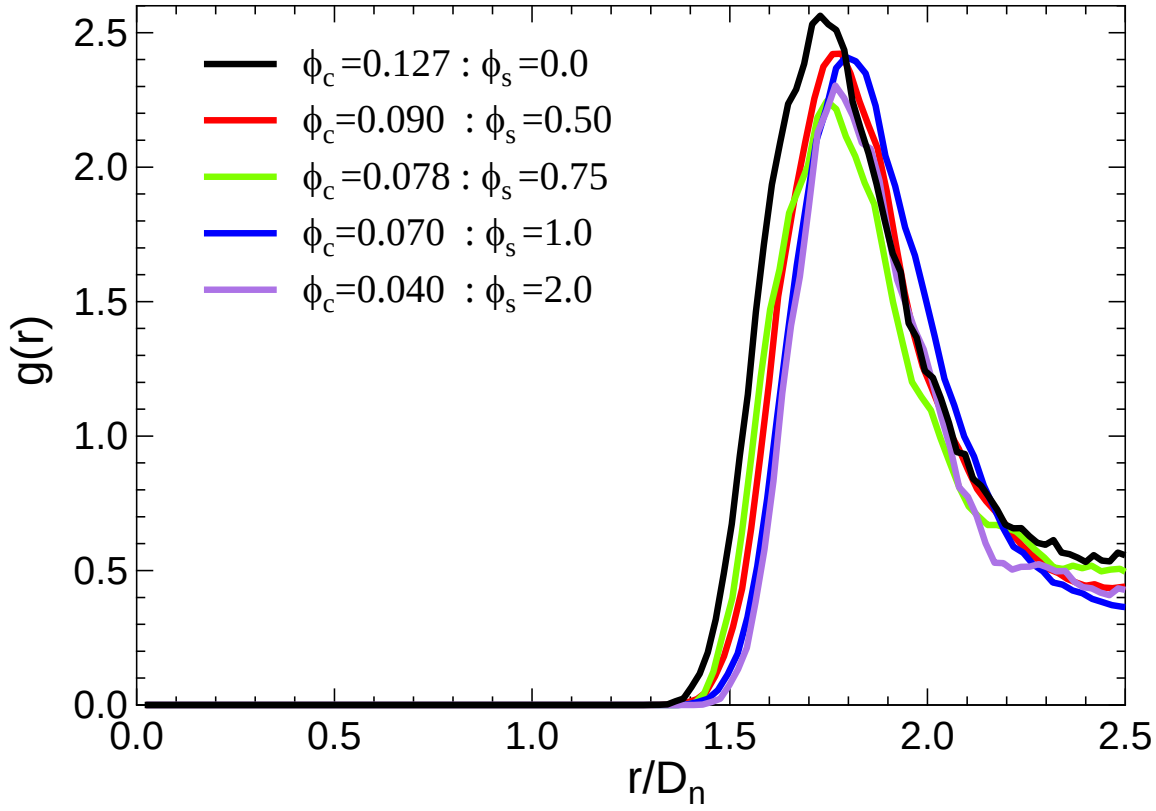

Figure 3.10 Radial distribution function of the PGNs with curvature 1.04 in the corona rich phase. The figure shows little change in the height of the first peak, indicative of similar neighboring core structure for all systems.

Due to phase separation, the limited size of the corona-rich domain reduces the maximum interparticle distances for which a "bulk" g(r) can be accurately estimated and hence only the first peak of the radial distribution function is plotted in Fig. 10. While in Figure 3.5 we observed that the first-peak height for the bulk radial distribution function increases upon dilution, in Figure 3.9 we see that the first peak height remains

constant in the corona-rich phase, indicating that the structure of the corona-rich phase for all systems is largely unchanged by dilution. The core volume fraction in the corona rich phase is found to be $\phi_c = 0.09$.

3.4.6 Phase Behavior

Using the above methods for characterizing phase separation, we simulate 4 additional systems with varying curvature ranging from ~0.35 to 1.29 (with the PGNs detailed in Table 1). We construct an approximate phase diagram of curvature vs. a metric of phase concentration which we define as $\frac{\phi_{phase}}{\phi_{pure}}$, where is the volume fraction of nanoparticles in each of the phases given by $\phi_{phase,i} = \frac{(number\ of\ cores\ in\ phase\ i)\times\frac{\pi}{6}D_n^3}{Volume\ of\ phase\ i}$, and ϕ_{pure} is the volume fraction of the solvent-free PGNs for each system. The normalized volume fraction reflects the concentration of nanoparticles distributed between each phase. Figure 3.11 shows the phase diagram of PGNs which demarks the regions of single-phase (well mixed) states and two-phase states. The circles represent the phase boundaries, squares depict the overall concentration of the systems which showed phase separated, and diamonds correspond to the systems which remained well mixed. Low curvatures and low $\frac{\phi_{phase}}{\phi_{pure}}$ are conditions that require very large simulation systems and are out of scope for this work and hence the plot is sparse in that region. For any system composition lying inside the two-phase region, the amount of corona-rich and solvent-rich phases can be calculated by the use of level arm rule. We observe that as curvature decreases, the difference between $\frac{\phi_{phase}}{\phi_{pure}}$ for corona-rich and solvent-rich phases also decreases and for curvatures below ~0.60, the system becomes well mixed for all

compositions. Figure 3.12 shows the normalized histogram for systems with curvature of 0.58 and 0.50. These are system that are close to the critical point in the phase diagram with the system with curvature 0.50, being the highest curvature system that is always well-mixed while the system with curvature of 0.58, is the system with lowest curvature which exhibits phase separation. It must be noted that the system with a curvature of 0.58 appears to phase separate into states with $\frac{\phi_{phase}}{\phi_{pure}}$ of 0.40 and 0.51 which are close on the phase diagram, however visually and through the density plots it is clearly a phase separated system. We find that the corona rich region covers 27% of the total volume of the system and contains 83 nanoparticles while the solvent rich region covers 73% of the total volume and contains 173 nanoparticles giving the reported concentration of each phase.

It must be noted that this phase diagram is valid only for $T^* = 1.0$ and $P^* = 0.1$.

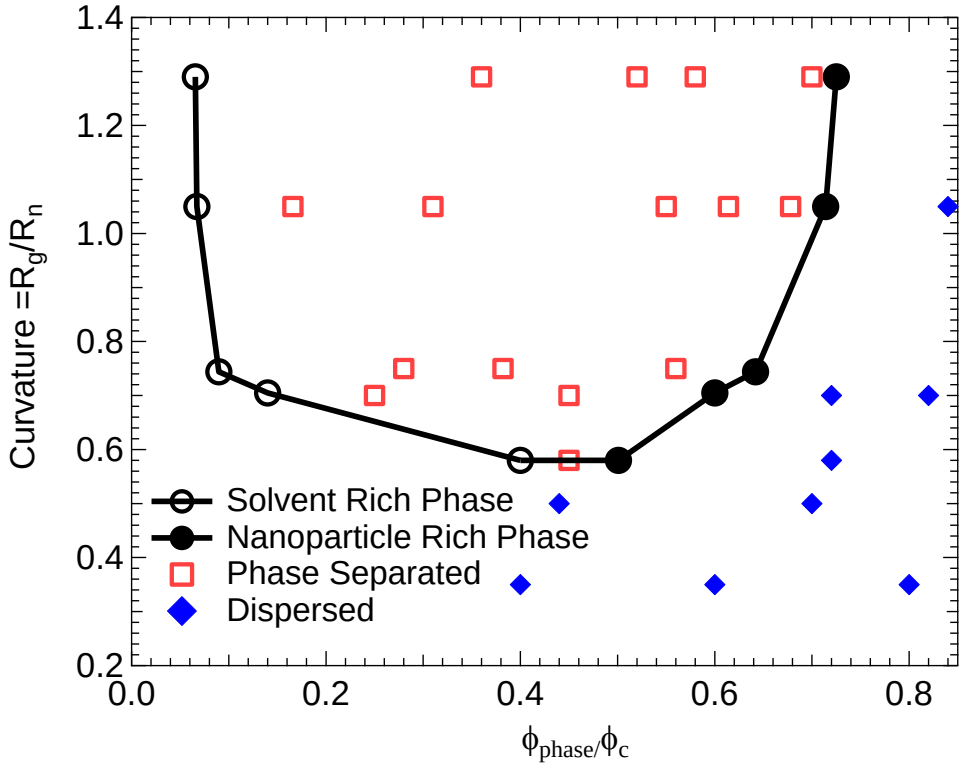

Figure 3.11. Phase diagram of PGN plus identical polymer solvent systems with PGN curvature plotted against the ratio of nanoparticle volume fraction (ϕ_{phase}) to volume fraction of solvent-free PGN's (ϕ_{pure}). The black line approximates the boundary between well mixed regions and phase segregated regions

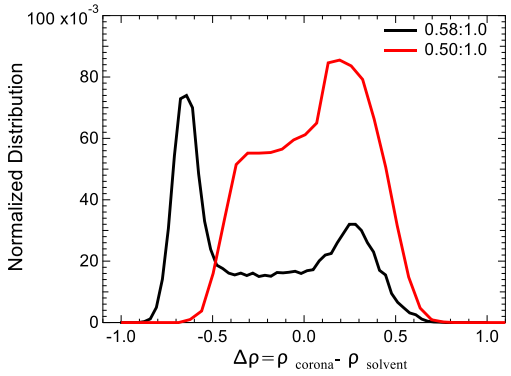

Figure 3.12. Normalized histogram for systems 0.58:1 and 0.50:1. The system with curvature 0.50 exhibits features of being well dispersed while the system with curvature 0.58 shows features consistent with phase separation.

To understand the effect of ratio of solvent chain length to grafted chain length on the phase diagram, we perform additional simulations for solvent chain length being 1.2 times larger than grafted chain length. Figure 3.13 shows the phase diagram for both cases, we observe that the increase the solvent length shifts the phase diagram lower and causes previously well mixed systems to phase separate. This can be explained by a more significant loss of conformational entropy when solvent is absorbed on the PGN corona leading to higher phase separation.

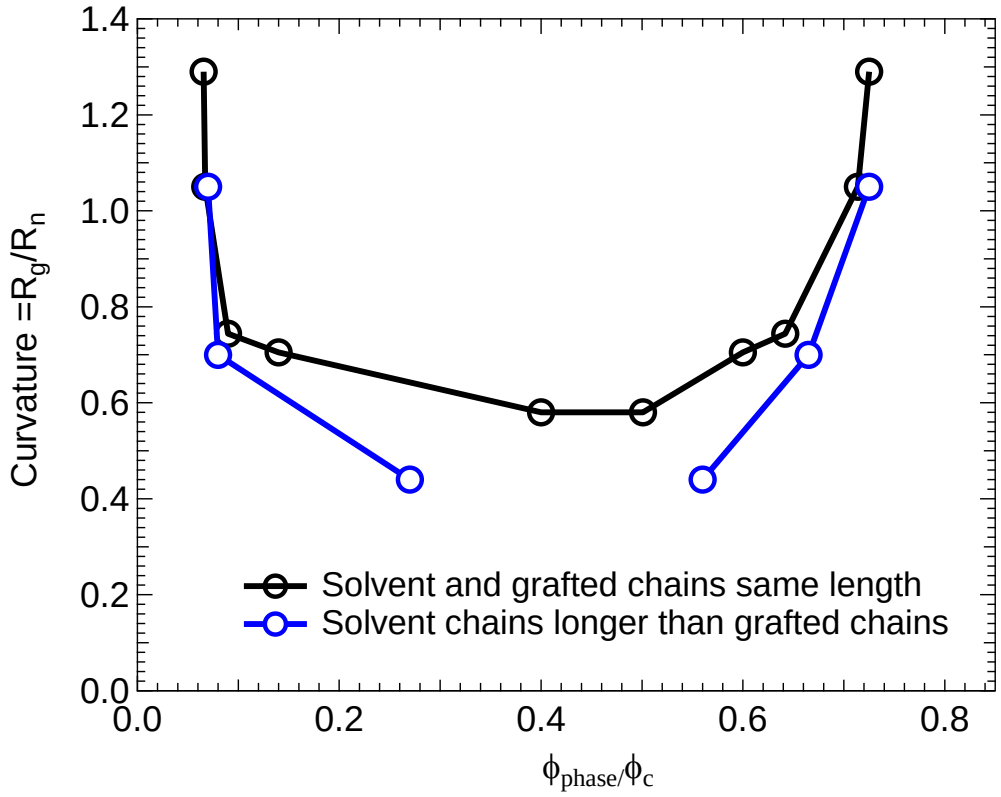

Figure 3.13. Phase diagram of PGN plus identical polymer solvent , and PGN plus polymer solvent 20% larger in length . The figure plots PGN curvature against the ratio of nanoparticle volume fraction (ϕ_{phase}) to volume fraction of solvent-free PGN's (ϕ_{pure}).

3.3.7 Scale of Phase Separation

Depending on the characteristic phase domain sizes, the observed phase separation could be microphase or macrophase separation. Microphase separation is observed in

some systems where the corona-rich phase separates to form morphologies (like sheets or strings) whose characteristic domain length is of microscopic size [46][i.e., of the order of a finite number of particles], while for macrophase separation, the two phases can attain macroscopic length scales. To gain more insight into this question, we performed an interfacial simulation with system 1.04:1 where an elongated box is used and as starting configuration, solvent-free PNGs are placed at one side of a planar interface and pure solvent is placed on the other as shown in figure 3.14. The simulation was run for 100τ with a bulk $\phi_c \sim 0.02$. After completion of the simulation, we find that the system remains phase separated with $\phi_c = 0.09$ in the corona rich phase and $\phi_c = 0.0083$ in the solvent rich phase, these values are identical with those calculated from the voxel decomposition approach described earlier and reported in the phase diagram of Fig. 3.11. Although the size of the simulated phases can only be as large as the simulation box, which is necessarily of microscopic size, these results, and the consistent trend observed in our phase diagram, suggest that macrophase separation does take place in our systems.

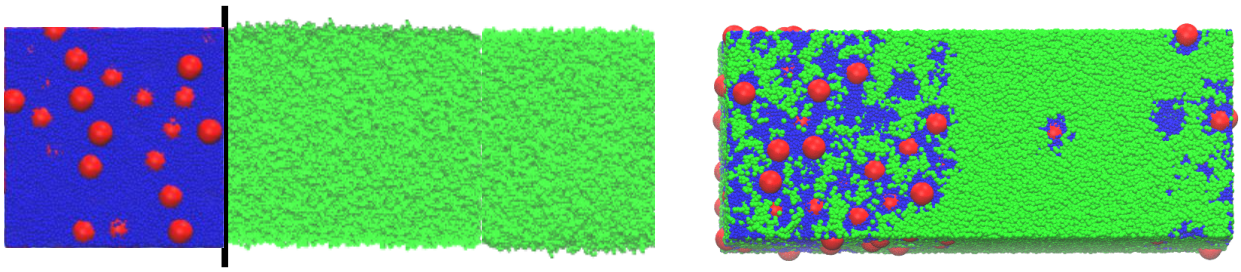

Figure 3.14. Two-phase interfacial set up for simulations of PGNs + solvent. (a) initial state having left region with solvent-free PGNs 1.04:0 and the right side with excess pure solvent. (b) final state of the system after equilibration

3.4 Conclusion

By using preparation protocols that favor phase separated states, we have shown that the curvature can greatly affect the phase behavior of PGNs, though in some cases the phases formed could be metastable. Low curvature PGNs have short polymers (relative to the particle radius) which are densely grafted to the particle surface and hence behave similarly as hard spheres, these expectedly form well dispersed dispersions in identical polymer solvent. The experimental results shown in figure 3.1 which lie with our simulation range consist of large nanoparticle with short grafted chains, these agree well with our results for low curvature where we expect well dispersed systems.

We observe a transition from well-mixed systems at low curvature values to phase separated systems at higher curvatures, and that the addition of solvent can cause some stable well-mixed systems to become phase separate. The measured diffusivity shows no change upon dilution for the phase separated PGNs; this result is consistent with what is expected for phase separation. For systems with overall concentration lying within the putative two-phase region, the variation of solvent content does not alter the

short-range radial distribution in the corona rich regions, suggesting a similar microstructure, and the density distribution plots only show changes in relative amounts of each phase. These indicators, together with visual analysis of system snapshots, allowed us to discriminate well-mixed and phase-separated states. For high curvatures, the relatively long grafted chains can swell significant when wetted by solvent chains. We speculate that due to the lack of enthalpic driving forces in our systems, the optimum solvent concentration that maximizes the entropy of the system varies with curvature. Once a suspension with ideal absorbed solvent has been created, on addition of further solvent, the increased wetting would decrease the translational entropy of the grafted chains and hence the systems would start to phase separate to maximize entropy. To confirm the entropic nature of this phase separation, we rerun simulations for the 1.04:1.0 system at fixed total volume with all LJ bead-bead interactions changed to be purely repulsive in nature via WCA potentials (which approximate hard-sphere interactions); this system only experiences excluded-volume (entropic) interactions and no enthalphic effects. As shown in Fig. 3.15, the snapshots show phase separation with corona rich phase having a volume fraction of $\phi_c = 0.09$ and solvent rich phase with $\phi_c = 0.0083$; these results are very similar to those of the regular model (shown in Fig. 3.5a), implying that the attractive interactions between the polymers is not the driving force for this phase separation. Interfacial simulations suggest that this phase separation is macroscopic in nature; however this result is restricted to the length scales used in these simulations.

These results probe the well-mixed phase-separated boundary and suggests that an intermediate region might exist between them. In this region, one can expect to observe

both well mixed and phase separated system depending on the preparation method and the metastable phase separated systems could be long lived. As the free energy difference is lower than $1k_BT$ between the well-mixed and phase-separated states, we expect that thermal fluctuations could be sufficient to force the material to transition between these states. Such transitions could result in some of the observed anomalous behaviors for soft materials. One such example is the puzzling hyperdiffusivity in which the material relaxation rate is proportional to the inverse of the wave function [77] or the power law governing MSD as a function of time has a power of greater than one. Such a phenomenon is observed in out of equilibrium systems and are driven by stress and density fluctuations in the system. Transition between equilibrium and metastable states could possibly be one of mechanisms by which such fluctuations are enhanced.

In our future work, we will focus on applying methods that will help us understand the free energy landscape associated with different systems and at conditions when seemingly stable phases-separated states and fully-mixed states can be produced via different preparation protocols. This will explain the stability of these phases in greater detail. Expanding the study to a wider P/N ratio would allow us to understand the complete phase diagram of PGNs and reveal the regions where metastable states can occur. It is also important to identify the origin of metastability and understand whether it is created due to geometric constraints or molecular mobility Such an understanding will help us intelligently design materials with desired properties.

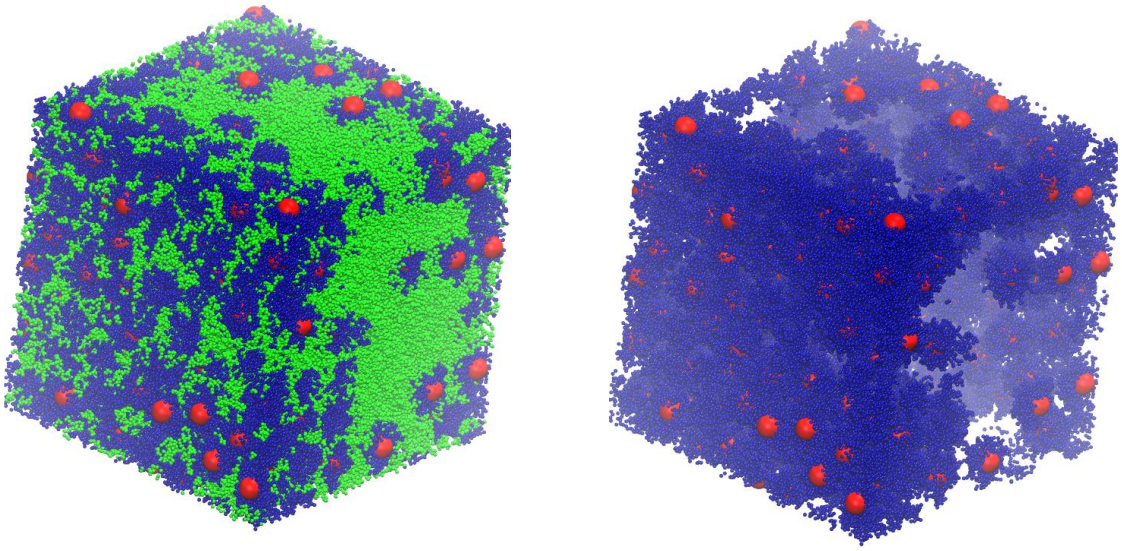

Figure 3.15. Snapshots of phase separated system with (ζ, Φ_s) = (1.04:1) for purely repulsive WCA potential. The figure on the left shows the nanoparticle cores and all chain beads in the system while the figure on the right only shows the cores and grafted corona beads.

4 Far-from-equilibrium sheared colloidal liquids: Disentangling relaxation, advection, and shear-induced diffusion

While ubiquitous across many time and length scales, far-from-equilibrium behavior is still an active field of study [1]. To understand such a behavior, the crossover between near -equilibrium systems to far-from-equilibrium regimes provides a useful bridge between both these limits. Furthermore, this poorly explored crossover is important for understanding natural phenomena such as nonlinear elasticity [2], flow-induced rejuvenation [3,4], and shear thinning [5–7], which all occur in industrial settings. A particularly fascinating and relevant example is the nonlinear stress response of fluids under large-amplitude oscillatory shear (LAOS) [8,9]. By varying the amplitude and frequency separately, LAOS disentangles the underlying dynamics that are usually convolved in such far-from-equilibrium systems.

Despite great efforts, conventional flow measurement techniques [10–14] have had difficulties elucidating the origins of these nonlinear behaviors without information about the fluid microstructure.

Because of their experimentally accessible time and length scales, hard-sphere colloids are an ideal model system to study nonlinear behaviors in far-from-equilibrium systems [15–17].

In this work, we use hard sphere potentials to perform Brownian dynamics simulations to understand the far from equilibrium behavior of colloidal systems.

4.2 Method

The interactions between hard-sphere colloids leading to the observed saturations can be mediated by either collisions or hydrodynamics. To determine whether particle collisions are sufficient to generate such saturations, we conduct dynamic simulations using the LAMMPS package (Sandia National Laboratory). We implement a Brownian dynamics simulation by applying a Langevin thermostat to the streaming velocity of simulated particles to maintain a constant temperature of $T*$ =1. The interparticle potential is taken to be $\frac{U}{k_B T} = r^{-c}$ with c varied from 12 (Lennard Jones potential) , 36 and finally 50. The pair potential stress is calculated using the virial equation.

4.3 Results

4.3.1 Brownian Stresses calculation

We found that the stress response for c = 50 agrees well with reported results for hard spheres in literature. The simulation setup contains 10 000 particles with φ = 0.28. We apply oscillatory shear to the system with the Lees-Edwards boundary condition.

Since the interparticle potential is very steep, the time step is carefully chosen to avoid unphysical particle overlaps. This model provides insights into the limiting physical behavior that ensues when pair- and higher-level hydrodynamic interactions are neglected. We run 100 oscillatory cycles for each $Deborah\ number = De = \frac{6\pi a^3 \omega \eta_0}{k_B T}$ and shear amplitude γ_0 and discard data obtained from the first 10 cycles as transient.

We perform an amplitude sweep at De = 15.7 for six different amplitudes and plot $\frac{\psi(t)}{\psi_0(\infty,\infty)}$ to compare with published experimental results for four different γ_0 and is shown in Fig. 4.1 (a). The quantity $\psi(t) =< \oint g(\vec{r},t)\hat{X}\hat{Y}d\Omega >$ is the structure signature and is a measure of the Brownian stress in the system. The term $\frac{\psi(t)}{\psi_0(\infty,\infty)}$ is the Brownian stress normalized by the stress obtained at infinite amplitude and frequency ($\psi_0(\infty,\infty)$). This is a metric used in experiments and hence useful to compare with current simulations. As recently shown in experiments, this model system also demonstrates an amplitude saturation at large γ_0,where $\frac{\psi(t)}{\psi_0(\infty,\infty)}$ deviates from the linear response. We also perform a frequency sweep for $0.20 \leq \gamma_0 \leq 4.00$ and plot the result for four different De at $\gamma_0 = 0.2$ plot the results for four of the six amplitudes in Fig. 4.1 (b). We find that the model system exhibits a similar saturation to that found in experiments. To determine whether similar data scaling can be applied to the numerical results, we plot the normalized value $\frac{\tilde{\psi}}{f(\gamma_0)}$ versus $\gamma 0\mathrm{De}/f(\gamma_0)$ in Fig. 4.2.

We find that the simulation data also collapse, but the curve's form deviates from the experimental curve at intermediate shear rates. Nevertheless, the collapse is qualitatively similar to the experimental results showing a linear response at low

shear rates and saturation at high shear rates. These results demonstrate that the interplay between Brownian relaxation, advection and shear-induced diffusion is sufficient to produce the observed saturations.

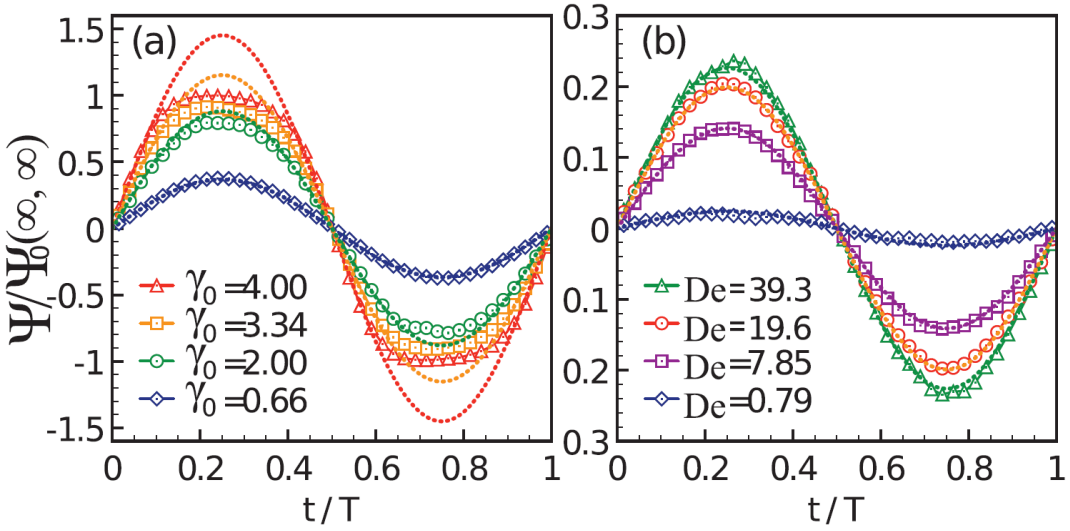

Figure 4.1 The normalized Brownian stress obtained from simulations. (a) Amplitude saturation for four different γ_0 at De=15.7 (b) Frequency saturation for four different De for $\gamma_0 = 0.20$

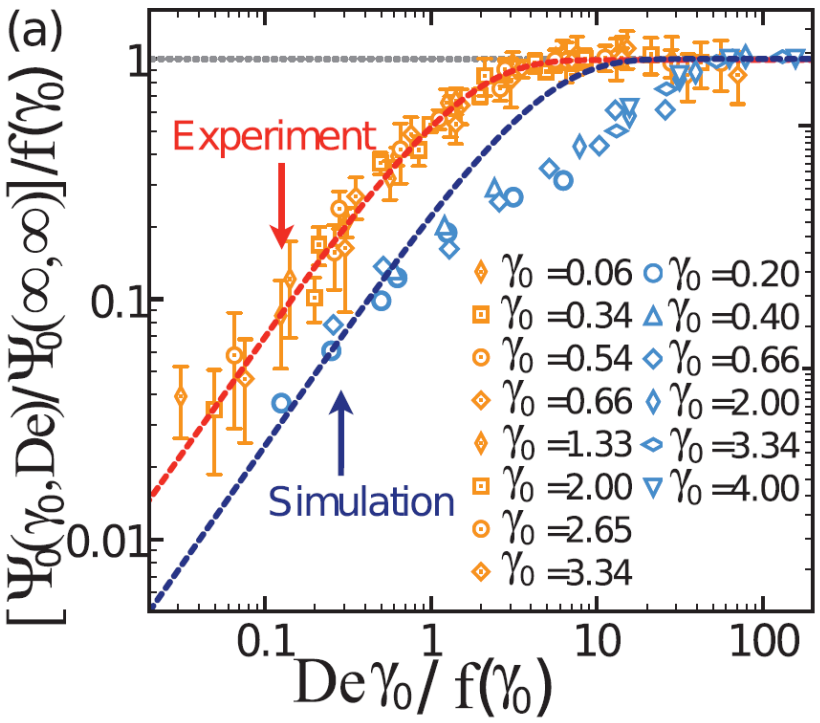

Figure 4.2. Plots a normalized Brownian stress against a normalized scaling parameter $De\gamma_0/f(\gamma_0)$. Each symbol denotes one strain amplitude for seven different De. All data collapse on a master curve that can be fit by an exponential saturation $1-e^{-\frac{\beta\gamma_0 De}{f(\gamma_0)}}$, where $\beta = 0.72$ is a fitting parameter.

4.3.2 Effect of the Interparticle Potentials

To examine whether the interparticle potential in Brownian dynamics simulations effectively mimics the hard-sphere potential, we calculate the shear stress XY for three different potentials: the Lennard-Jones potential, U ∝ r−36, and U ∝ r −50. The results of all three different potentials are plotted along with the data reproduced from previous

simulation results [19] in Fig. 3. For the reproduced data, we determine the corresponding stresses by multiplying the η value plotted

in Ref. [19] by Pe/6πr3. To examine whether the interparticle potential in Brownian

dynamics simulations effectively mimics the hard-sphere potential, we calculate the shear stress XY for three different potentials, namely, the Weeks-Chandler-Andersen (WCA) Lennard-Jones-based (LJ) potential, U ∝ r−36, and U ∝ r −50.

Figure 4.3 shows the results of all three different potentials

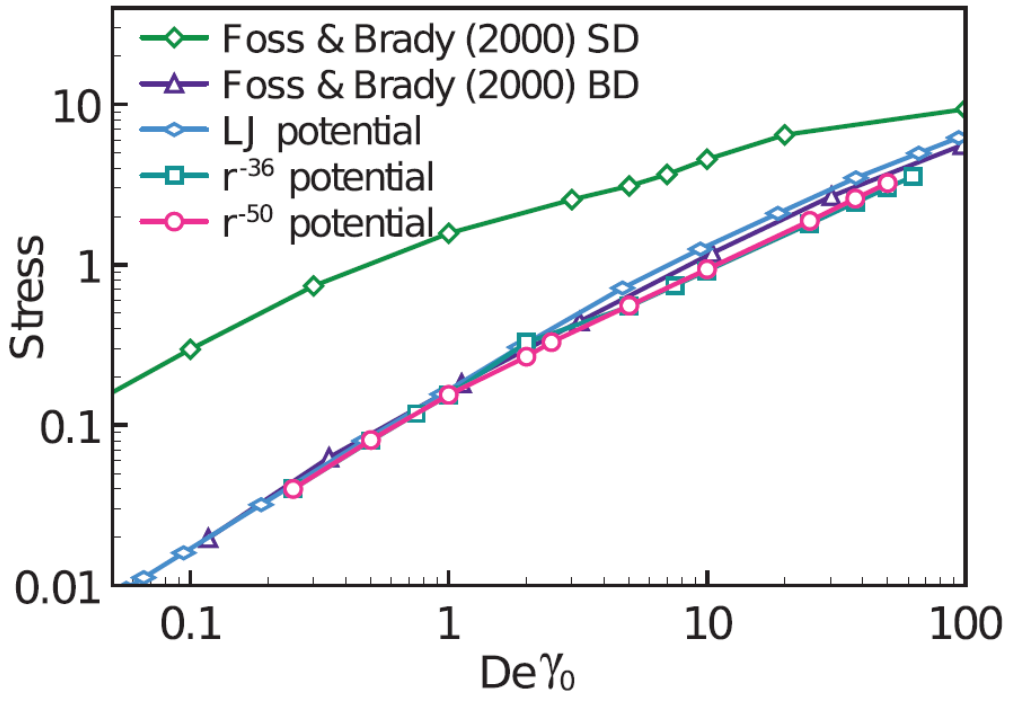

Figure 4.3 Stress responses in different simulation plotted versus $De\gamma_0$. The data points of SD and BD are the Stokesian dynamics simulations ($\phi = 0.45$) and Brownian dynamics simulations ($\phi = 0.30$) from literature.

plotted along with data from previously reported simulation results for hard spheres [19] (for the latter we determine the corresponding stresses by multiplying the reported η value by Pe/6πr3).We find that when the steepness of the repulsive branch

of the potential is increased from the WCA Lennard-Jones potential ($U \propto r-12$) to $U \propto r-36$, the stress response is quantitatively similar at small $De\gamma_0$ and deviates very slightly at $De\gamma_0 > 10$. As the potential steepness is increased from $U \propto r^{-36}$ to $U \propto r^{-50}$, the stress remains quantitatively similar at all $De\gamma_0$. This shows that the $U \propto r^{-36}$ and $U \propto r^{-50}$ potentials can both be considered very good approximations to the hard-sphere potential. The stress outputs from both potentials also nearly match the resulting stress from previous

Brownian dynamics simulations, which use a different algorithm to generate the hard-sphere potential [19]. Results from Stokesian dynamics simulations for hard-sphere suspensions are also available, but for a packing fraction of 0.45 [19], which is larger than the 0.30 used in the Brownian dynamics simulations. Under such conditions, the calculated stress from Stokesian dynamics is approximately one order of magnitude

larger than that found for the Brownian dynamics simulations at small Deγ0. At large Deγ0, the stress from Stokesian dynamics simulations appears to saturate, while the stress in Brownian dynamics simulation keeps increasing with nearly

constant rate [19].

4.4 Conclusion

We have been able to qualitatively reproduce the experimental results that show saturation of Brownian stress for colloidal systems at high oscillation frequency and amplitude. We though find that the method followed by experiments which involve integral of g(r) shows saturation while the actual stress does not saturate. This could be due to either the error in the results due to saturation or due to lack of explicit hydrodynamics. It would be interested to look at the results from Stokesian dynamics under confinement to know the answer.

5 Conclusions

In this work we have used computational models to understand the structure, rheology and the phase behavior of PGNs to gain insight into engineering better materials for various applications. Our models serve as a good complement to experiments, DFT and PRISM theory, and atomistic simulations. The trends that molecular dynamics predict can serve as useful guidelines and shed light on enthalpic and entropic phenomenon. A common problem with coarse grained simulations is the inaccurate representation of time scale and length scale but use of correct dimensionless comparisons have shown to yield satisfactory results.

Some of the phenomenon like long time diffusivity for testing non-linear dynamics and true macroscale phase separation has not been possible but the increase in computational capabilities with clusters like XSEDE, and improvements in software's like LAMMPS and GROMACS which can be run in parallel efficiently in on thousands of cores, simulations of larger systems, and time scales have been made possible. Furthermore, multiscale approaches have the potential of using atomistic information to provide macroscale results.

5.1 Summary and Conclusions

We have created a mesoscale model using which we have been able to reproduce experimental properties and suggest mechanism for observed experimental and theoretical trends. We studied the microstructure, equilibrium diffusivity, and response to stress of PGNs for various grafting density, grafted chain length and core volume fraction. Comparing a system of pure PGNs with one in which a single PGN is infinitely diluted in an oligomer identical to the grafted chains, we found that the translational motion is greatly reduced due to the caging by neighboring PGNs, while rotational motion is only mildly reduced due to the lower mobility of the grafted oligomers. We found that shorter grafted chains results in a more structured distribution reducing the translational motion due to caging of the nanoparticles while the rotation was unaffected. Simulations of uniaxial stretching show that systems with longer chains exhibit liquid bridge like structure during breakup. However, a system with equal core volume fraction but shorter grafted chains exhibits soft-glass-like fracture.

We also observed that for a fixed grafted chain length N_m, reduction in grafting density leads to a non-trivial core structure where nanoparticles get in close contact promoting faster translational and rotational diffusivities. Such close contacts also lead to low-GD systems to be less viscous than high-GD systems, a trend that is reversed as the shear rate is increased and the structure made more homogeneous.

On application of constant shear rate, all systems exhibit shear thinning with the shear thinning slope for solventless PGN's being larger than that for solvated PGN's which was in turn larger than theoretical limit of bare nanoparticles suspended in fluid with

same ϕ_c. Calculation of yield stress using constant stress ensemble reveals consistent results with constant strain rate simulations and also reveals that blends do not reveal a clear yielding signature.

On studying the molecular origin of the observed shear thinning, we find that although Browning stresses decrease with shear rate, their contribution to viscosity is minimal at the Peclet number simulation and hence could not be the driving force behind shear thinning. On examining the extent of polymer chain alignment under shear, we find that systems with more uniformly dispersed corona tend to align more in direction of shear, giving a possible mechanism for the lower viscosity of PGNs with longer chains. We also find that grafted chains align more in the direction of shear when compared to free chains and hence could be the reason for a larger shear thinning slope for pure PGNs. Finally, we observed a residual chain alignment present in PGNs due to the shear-induced non-equilibrium distribution of cores, which would also affect the stress response of PGNs.

When compared to more coarse grained models like soft-sphere pair potentials or Gaussian-core potentials, our more detailed PGN model, allows us to account for other effects that are associated with multibody intra- and inter-chain interactions, and with intrinsic or dynamic spatial anisotropies of the corona. Properties such as corona distribution, interdigitation, rotational diffusivity, chain alignment under shear required explicit polymer chains and are excellent properties for mesoscale models.

On comparing results for flat surfaces grafted with polymer and PGNs, we found that curvature plays a key role in defining the phase behavior of densely grafted PGNs. To

isolate the effect of curvature on the phase behavior we fix the grafting density and the solvent is kept identical to the grafted polymer. For systems with low curvature, we find that on visual inspection the system in well mixed for all amounts of solvent. We find that the peak of radial distribution function, first increases on dilution and then decreases. We attribute this phenomenon which is also observed in experiments to the gain in rigidity of the grafted corona upon wetting with solvent.

For medium curvature PGNs we observe that for well dispersed systems, addition of solvent causes the system to phase segregate into a corona rich and a solvent rich phase. When radial distribution function for high curvature systems was calculated, we find that bulk g(r) shows an anomalous trend where its first peak height increases upon dilution. This contradicts colloidal behavior as addition of solvent should increase the interparticle distance and hence decrease the peak. We attribute this to phase separation as on calculating the nanoparticle rich g(r), we find that the height of the first peak remains constant. To ensure that these trends are not an artifact of monodisperse systems, we apply high polydispersity to grafted chains and observe no change in behavior.

Using density difference between grafted and solvent chains, we were able to identify both phases in the system. On calculation the diffusivity of the nanoparticle rich phase, we find that addition of solvent does not affect the diffusivity as the interparticle distance and dynamics do not change with solvent quantity. By calculating the amount of each of the phase and extending this method to further systems, we were able to obtain a phase diagram that relates curvature to the regions which phase separate and

regions which are well mixed. Simulations with purely repulsive WCA potential reproduce the same result confirming that the phase separation is a purely entropic phenomenon and we speculate it is driving by the mixing entropy of solvent chains and grafted chains.

Interface simulations reveal that for simulation length scale, the phase separation is macroscopic in nature.

5.2 Future Work

There are multiple questions which can be answered by the use of simulations, some of them are

1) Now that the effect of curvature, grafting density and polymer chemistry has been studied independently, identification of critical points for well mixed and phase separated regions will be critical
2) The effect of shear on phase behavior will reveal more information about the magnitude of driving force for phase separation
3) PGNs studied can be looked as diblock systems of silica and polymer. Extending this work to triblocks can lead to very interesting morphologies and phase behavior
4) Multiscale modeling will be essential to capture some of the large time and length scale phenomenon like Newtonian viscosity and hyperdiffusivity

References

[1] R. Krishnamoorti and R. A. Vaia, J. Polym. Sci., Part B: Polym. Phys. **45**, 3252 (2007).

[2] A.B. Bourlinos, S. R. Chowdhury, R. Herrera, N. Chalkias, D. D. Jiang, L. A. Archer and E. P. Giannelis, Adv. Funct. Mater. **15**, 1285 (2005).

[3] P. Agarwal, H. Qi, and L.A. Archer, Nanolett. **10**, 111 (2010).

[4] R. Rodriguez, R. Herrera, L.A. Archer, and E.P. Giannelis, Adv. Materials **20**, 4353 (2008).

[5] H.-Y. Yu and D. Koch, Langmuir **26**, 16801(2010).

[6] L. A. Archer and D. Kim, Langmuir **27**, 3083 (2011).

[7] D.L. Green and J. Mewis, Langmuir **22**, 9546 (2006).

[8] A. Jayaraman and K.S. Schweizer, Macromolecules **42**, 8423 (2009).

[9] A. Jayaraman, and K.S. Schweizer, J. Chem. Phys. **128**, 164904 (2008).

[10] M.E. Mackay, A. Tuteja, P. M. Duxbury, C. J. Hawker, B. V. Horn, Z. Guan, G. Chen, R. S. Krishnan, Science **311**, 1740 (2006).

[11] P. Akcora , H. Liu, S.K. Kumar, J. Moll, Y. Li, B. C. Benicewicz, L. S. Schadler, D. Acehan, A. Z. Panagiotopoulos, V. Pryamitsyn, V. Ganesan, J. Ilanvsky, P. Thiyagarajan, R. H. Colby and J. F. Douglas, Nature Mat. **8**, 354 (2009).

[12] A. Chremos and A.Z. Panagiotopoulos, Phys. Rev. Lett. **107**, 105503(2011).

[13] M. P. Allen and D. J. Tildesley, *Computer simulations of Liquids* (Oxford university press, New York 1987), Chap. 8.

[14] H. C. Andersen, J. Chem. Phys. **72**, 2384 (1980).

[15] M. G. Mazza , N. Giovambattista, F. W. Starr and H. E. Stanley, Phys. Rev. Lett. **96**, 2 (2006).

[16] R. A. Reis, F. C. Silva, R. Nobrega, J. V. Olivera, F. W. Tavares, Fluid Phase Equilibria **221**, 25 (2004).

[17] S.-H. Chong and W. Kob, Phys. Rev. Lett. **102**, 1 (2009).

[18] A. Z. Akcasu, N. Corngold, and J.J. Duderstadt, Phys. Fluids **13**, 2213 (1970).

[19] A. R. C. Baljon and M.O. Robbins, Comput. Theoretical Polymer Sci. **9**, 35 (1999).

[20] J. Rottler, S. Barsky, and M. O. Robbins, Phys. Rev. Lett. **89**, 148304 (2002).

[21] S. W. Sides, G. S. Grest, M. J. Stevens, S. J. PlimptonJ. Polymer Sci.: Part B: Polymer Physics **42**, 199 (2004).

[22] R. Edberg, D. J. Evans, and G. P. Morriss, J. Chem. Phys. **84**, 6933 (1986).

[23] R. Edberg, D. J. Evans, and G. P. Morriss, J. Chem. Phys. **86**, 4555 (1987).

[24] A. W. Lees and S. F. Edwards, J. Phys. Chem.: Solid State Phys. **5**, 1921 (1972).

[25] L. M. Hood, D. J. Evans, and G.P. Morriss, Mol. Phys. **62**, 419 (1987).

[26] J. F. Brady, J. Chem. Phys. **98**, 3335 (1993).

[27] J. F. Brady, J. Chem. Phys. **99**, 567 (1993).

[28] D. R. Foss and J. F. Brady, J. Fluid Mech. **407**, 167 (2000).

[29] F. Rodriguez, C. Cohen, C. K. Ober and L. A. Archer, *Principles of Polymer Systems*, 5th ed. (Hemishphere Pub., New York, 2003).

[30] M. Doi and S. F. Edwards, *Theory of Polymer Dynamics*, 1st ed. (Oxford Science Pub., Oxford, 1986).

[31] W.P. Krekelberg, T. Kumar, J. Mittal, J.R. Errington and T.M. Truskett, Phys. Rev. E **80**, 061205 (2008)

[32] M.J. Pond, J.R. Errington and T.M. Truskett, J. Chem. Phys. **134**, 081101, (2011)

[33] M.J. Pond, J.R. Errington and T.M. Truskett, Soft Matter, Advanced Article (2011)

[34] N. Tsubokawa, J. Polym. **39**, 983(2007).

[35] S. Sen, Y.P. Xie, S.K. Kumar, H.C. Yang, A. Bansal, D.L. Ho, L. Hall, J.B. Hooper, K.S. Schweizer, Phys. Rev. Lett. **98**,128302 (2007)

[36] M.K. Corbierre, N.S. Cameron, M. Sutton, K. Laaziri, R.B. Lennox, Langmuir. **21**, 6063(2005)

[37] B.J. Kim, J. Bang,C. J. Hawker, E. J. Kramer, Macromolecules. **39**, 4108(2006).

[38] Q. Lan, L. F. Francis, F. S. J. Bates, Polym. Sci., Part B: Polym. Phys. **45**, 2284(2007).

[39] A. Jayaraman, Polym. Sci., Part B: Polym. Phys. **51**, 524 (2013)

[40] A. L. Frischknecht, A. Yethiraj, , J. Chem. Phys., **134**, 174901(2011)

[41] T.B. Martin, A. Jayaraman, Macromolecules. **46**, 9144(2013).

[42] E.S. McGarrity, A.L. Frischknecht, L.J.D. Frink, M. Mackay, Phys. Rev. Lett. **99**, 23802 (2007)

[43] P.F. Green, Soft Matter. **7**, 7914(2011).

[44] K.R. Shull, J. Chem. Phys. **94**, 5723(1991).

[45] S.E. Harton, S.K. Kumar, J. Polym. Sci., Part B: Polym. Phys. **46**, 351(2008).

[46] S.K. Kumar,N. Jouault, B. Benicewicz,T. Neely, Macromolecules. **46**, 3199(2013).

[47] C. Chevigny, F. Dalmas, E. Di Cola, D. Gigmes, D. Bertin, F. Boue, J. Jestin, Macromolecules. **44**, 122(2011).

[48] D. Sunday, J. Llavsky, D.L. Green, Macromolecules. **45**, 4007 (2012)

[49] S. Srivastava, J. L. Schaefer, Z. Yang, Z. Tu, L.A. Archer, Adv. Mater. **26,** 201 (2014)

[50] S. Srivastava, P. Agarwal, L.A. Archer, Langmuir. **28**, 6276 (2012)

[51] N. Nair, N. Wentzel, A. Jayaraman, J. Chem. Phys. **134**, 194906(2011).

[52] A. Rungta, B. Natarajan, T. Neely, D. Dukes, L.S. Schadler, B.C. Benicewicz, Macromolecules. **45**, 9303(2012).

[53] B. Natarajan, T. Neely, A. Rungta, B.C. Benicewicz, L.S. Schadler, Macromolecules. **46**, 4909(2013).

[54] B. Lin, T.B. Martin, A. Jayaraman, ACS Macro Lett. **3**, 628(2014)

[55] T.B. Martin, K.I.S. Mongcopa, R. Ashkar, P. Butler, R. Krishnamoorti, A. Jayaraman, J. Am. Soc. **137**,10624(2015)

[56] I. Borukhov, L. Leibler, Macromolecules. **35**, 5171(2014)

[57] I. Borukhov, L. Leibler, Phys. Rev. E: Stat. Phys., Plasmas, Fluids, Relat. Interdiscip. Top. **62**, R41(2000).

[58] C.F. Laub, J.T. Koberstein, Macromolecules. **27**, 5016(1994).

[59] M. Muller, L.G. MacDowell, Europhys. Lett. **55**, 221(2001).

[60] B. Kim, D.Y. Ryu, V. Pryamitsyn, V. Ganesan, Macromolecules. **42**, 7919(2009)

[61] R. Hasagawa.,Y. Aoki., M. Doi. Macromolecules. **29**, 6656(1996)

[62] L. Yezek, W. Schartl, Y. Chen, K. Gohr, M. Schmidt, Macromolecules. **36**, 4226(2003)

[63] V. Ganesan, A. Jayaraman, Soft Matter. **10**, 13(2014).

[64] C. Xu, K. Ohno, V. Ladmiral, R. Composto, J. Polymer. **49**, 3568(2008).

[65] S. Khani, S. Jamali, A. Boromand, M.J.A. Hore, J. Maia, Soft Matter. **11**, 6881 (2015)

[66] T. Lafitte, S.K. Kumar, A.Z. Panagiotopoulous, Soft Matter. **10**, 786 (2014)

[67] D. Meng, S.K. Kumar, J. M. D. Lane, G.S. Grest, Soft Matter. **8**, 5002 (2012)

[68] S. Plimpton, J. Comp Phys. **117**, 1(1995)

[69] D. Trombly, V. Ganesan, J. Chem. Phys. **133**, 154904 (2010)

[70] S. Goyal, F. Escobedo, J. Chem. Phys. **135,**184902 (2011)

[71] T. Soddermann, B. Dunweg, K. Kremer, Physical Review E. **68,** 046702 (2003)

[72] S. Srivastava, L. A. Archer, S. Narayanan Phys. Rev. Lett. **110**, 148302 (2013)

[73] Stephen Z.D. Cheng, Elsevier, 2008, Phase Tansitions in Polymers : The Role of Metastable States

[74] S. Cheng, A. Keller, Annu. Rev. Mater. Sci. **28,** 533-662(1998)

[75] V. J. Anderson, H.N.W. Lekkerkerker, Nature **416**, 811-815(2002)

[76] A. Agarwal, B. M. Wenning, S. Choudhary, L.A. Archer, Langmuir, **32**, 34(2016)

[77] S. Srivastava, P. Agarwal, R. Mangal, D. L. Koch, S. Narayana, L.A. Archer, ACS Macro Lett. **4**, 1149-1153 (2015)